MICROCOPY RESOLUTION TEST CHART
NATIONAL BUREAU OF STANDARDS-1963-A

CRREL
REPORT 85-5

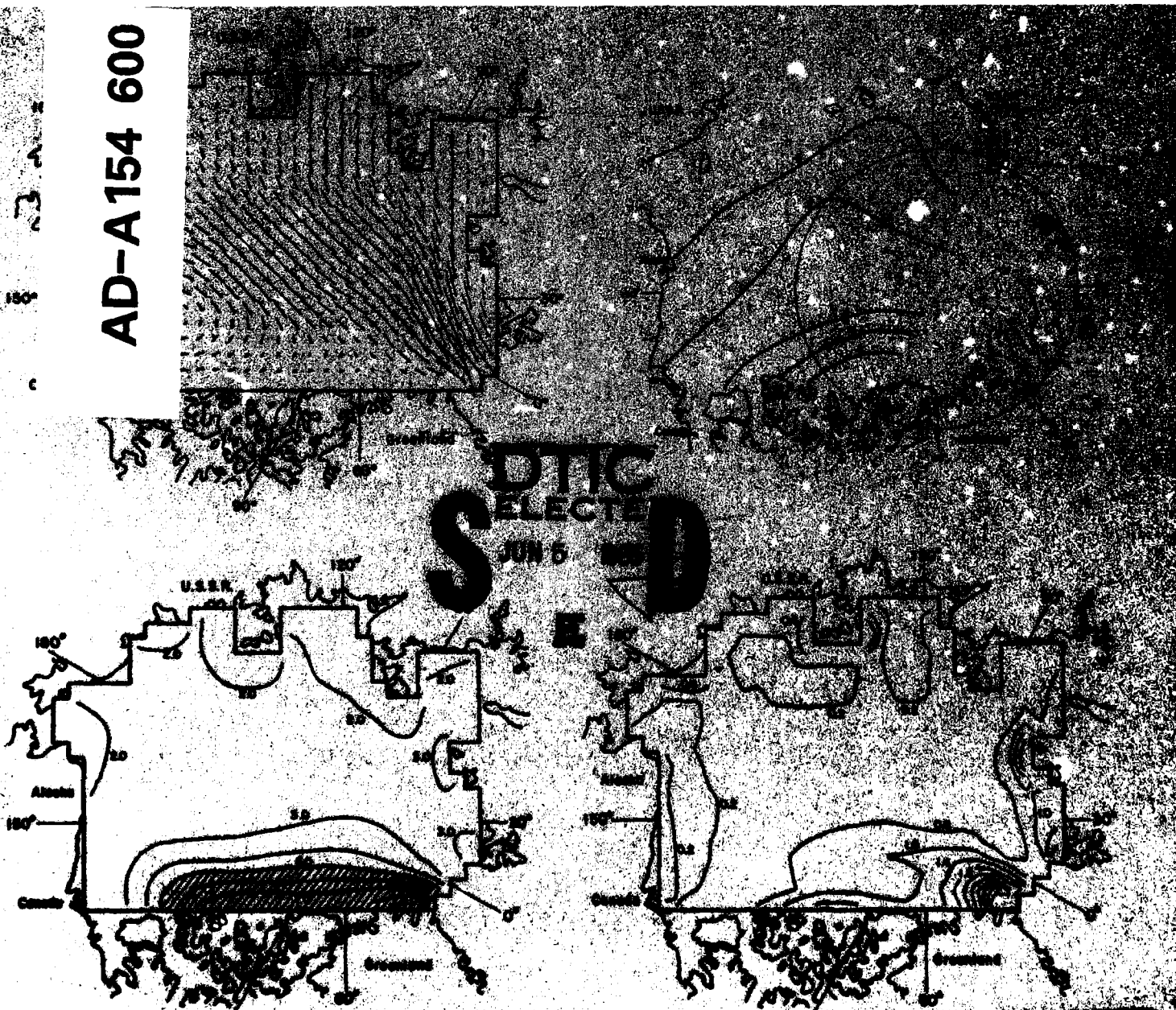**US Army Corps of Engineers**
Cold Regions Research &
Engineering Laboratory

Numerical modeling of sea ice dynamics and ice thickness characteristics
A final report

Cover: Simulated average annual ice velocity field (top left), approximate contours of observed ice thickness values (top right), simulated average ice thickness contours for April (bottom left), and contours of simulated volume of deformed ice per unit area for one annual cycle (bottom right). All contours in metres.

CRREL Report 85-5

March 1985

Numerical modeling of sea ice dynamics and ice thickness characteristics
A final report

William D. Hibler III

Accession For

NTIS GRA&I
DTIC TAB
Unannounced
Justification

By
Distribution/

Availability Codes

Dist | Avail and/or
     | Special

A/1

REPORT DOCUMENTATION PAGE		READ INSTRUCTIONS BEFORE COMPLETING FORM
1. REPORT NUMBER CRREL Report 85-5	2. GOVT ACCESSION NO. AD--1154 E(K)	3. RECIPIENT'S CATALOG NUMBER
4. TITLE *(and Subtitle)* NUMERICAL MODELING OF SEA ICE DYNAMICS AND ICE THICKNESS CHARACTERISTICS A Final Report		5. TYPE OF REPORT & PERIOD COVERED
		6. PERFORMING ORG. REPORT NUMBER
7. AUTHOR(s) William D. Hibler III		8. CONTRACT OR GRANT NUMBER(s)
9. PERFORMING ORGANIZATION NAME AND ADDRESS U.S. Army Cold Regions Research and Engineering Laboratory Hanover, New Hampshire 03755		10. PROGRAM ELEMENT, PROJECT, TASK AREA & WORK UNIT NUMBERS
11. CONTROLLING OFFICE NAME AND ADDRESS Office of Naval Research, Arlington, Virginia 22217		12. REPORT DATE March 1985
		13. NUMBER OF PAGES 60
14. MONITORING AGENCY NAME & ADDRESS*(if different from Controlling Office)*		15. SECURITY CLASS. *(of this report)* Unclassified
		15a. DECLASSIFICATION/DOWNGRADING SCHEDULE

16. DISTRIBUTION STATEMENT *(of this Report)*

Approved for public release; distribution is unlimited.

17. DISTRIBUTION STATEMENT *(of the abstract entered in Block 20, if different from Report)*

18. SUPPLEMENTARY NOTES

19. KEY WORDS *(Continue on reverse side if necessary and identify by block number)*

Arctic Basin ice cover	Sea ice
Arctic Ocean	Simulation modeling
Mathematic models	

20. ABSTRACT *(Continue on reverse side if necessary and identify by block number)*

A dynamic-thermodynamic sea ice model is extended to include a full thermodynamic code and a complete multilevel ice thickness distribution. The variable thickness formulation includes a more realistic parameterization of ice ridging than used in previous models. Seasonal simulations have been performed using this model and the results have been analyzed with particular emphasis on examination of the ridge buildup results off the Canadian Archipelago and off the North Slope. This report presents a complete description of this model and discusses progress made on examining and testing the variable thickness extensions.

DD FORM 1473 EDITION OF 1 NOV 65 IS OBSOLETE

PREFACE

CONTENTS

ILLUSTRATIONS

TABLES

Table

SUMMARY

The main objective of this research is the development and verification of numerical models for simulating the dynamic and thermodynamic characteristics of the Arctic ice cover. Emphasis has been placed on realistically parameterizing the ridging process within the framework of a variable thickness sea ice model.

The basic model consists of a multiple-level ice thickness distribution coupled to a complete momentum balance employing a viscous plastic constitutive law. A flow chart describing the overall model is given in Figure 1. Note that a full heat budget code, a fixed depth oceanic mixed layer, and a sea ice thermodynamic model are used in conjunction with the ice thickness evolution equations. Details of the equations are presented in the main text. In the numerical code, the ridge redistribution process is formulated in a general manner so that a variety of different ridging mechanisms may be modeled. The numerical scheme is formulated in a fixed Eulerian grid so that integrations over unlimited time intervals may be performed. In addition, in the mixed layer formulation, lateral melting terms are included. In the computer code, special attention has been given to conservation properties. Specifically, the code is formulated to manifestly conserve air–sea heat exchanges so that all energy exchanges are precisely accounted for in terms of ice formation, ice melt or warming of the oceanic mixed layer. Because of these conservation properties, the code is suitable for coupling to atmospheric and oceanic general circulation models.

Because of the importance of ridging in this model, considerable effort has gone into designing a realistic ridge distribution process. To this end a redistribution process consistent with observed and hypothesized physics of the ridging process is proposed. This redistributor is analytically examined and compared to a previous proposed redistributor (Fig. 3 and 4). The two key physical features incorporated in this redistributor are 1) under deformation, ridging transfers ice to a variety of thickness categories, 2) typical ridge heights increase more slowly than does the thickness of ice being ridged. Analytic calculations show that taking into account the second feature tends to preferentially increase thin ice strengths as compared to previously proposed redistributors (Fig. 4).

The main approach to analyzing the fully coupled model characteristics has been to carry out an equilibrium variable thickness simulation of the Arctic Basin ice cover. In this simulation, a plastic rheology coupled to a 10-level ice thickness distribution was found to yield realistic geographical variations in ice thickness, with ice in excess of 7 m thick along the Canadian Archipelago and about 2 m along the Alaskan North Slope (Fig. 7). Examination of this buildup shows that it takes several years to fully evolve and is largely due to ridging.

The volume of ridged ice formed each year also shows interesting spatial variations (Fig. 11). The general shapes of the roughness contours in this figure agree well with surface roughness observations. The major feature is a heavy buildup of ridging off the Canadian Archipelago together with less ridging near the pole. In addition, there is a zone of heavy ridging just off the North Slope that is in agreement with observations there. A final feature is a tongue of high ridging further offshore near the tip of Greenland. Roughness data obtained from submarine profiles also show such a tongue.

Several sensitivity experiments were performed to determine the major factors dictating the ice edge location (Fig. 7, 13, and 14). The results indicate that it is a combination of summer melt coupled with large amounts of offshore advection early in the spring. The most critical factor, however, appears to be summer melt. An increase in the albedo of melting ice by only 10%, for example, substantially improved the results from North Slope ice edge (Fig. 13).

The results also give some insight into strengths needed for proper simulations. Basically, by use of the ridging parameterization mentioned above, a realistic ice buildup was simulated. However, the simulated ice velocities were rather large (Table 1). Sensitivity analyses suggest that a modest increase in frictional losses would be adequate for obtaining more realistic ice velocities and strengths. Further, more detailed studies with polar drifting buoys are needed to more precisely determine these strengths.

With regard to future research, substantial progress has been made on the development and numerical examination of a complete variable thickness sea ice model. However, considerable theoretical and numerical work remains to determine more precisely the strengths and weaknesses of this model as it stands. The ice dynamics formulation, particularly, needs further study.

NUMERICAL MODELING OF SEA ICE DYNAMICS AND ICE THICKNESS CHARACTERISTICS
A Final Report

William D. Hibler III

INTRODUCTION

In the polar regions the interaction between the atmosphere and the ocean is significantly modified by the presence of a sea ice cover. Typically, this ice cover contains a variety of ice thicknesses that evolve in response to both dynamic and thermodynamic forcing. This variable thickness feature can substantially change the way the ice cover modifies the air-sea interaction and, hence, affect the atmospheric and oceanic circulation. Numerical and empirical studies demonstrating the relevance of this interaction to the atmosphere have recently been carried out by Herman and Johnson (1978), Walsh and Johnson (1979a), Saltzman and Moritz (1980), Lemke et al. (1980) and Manabe and Stouffer (1980). In light of these results, properly simulating a variable thickness sea ice cover has become particularly relevant to numerical investigations of climate.

Recent research on modeling a variable thickness ice cover is largely based on pioneering work by Coon (1974), Thorndike et al. (1975) and Rothrock (1975). Specifically, Thorndike et al. (1975) introduced an areal ice thickness distribution function and developed equations for the dynamic-thermodynamic evolution of this distribution. The input fields for the evolution equations consist of a two-dimensional ice velocity field and ice growth rates versus thickness and time. In this model the effects of ice dynamics on the ice thickness distribution are quantified by allowing thin ice formation and redistribution of ice to thicker categories (because of ridging) in response to deformation. Similarly, thermodynamic effects cause a rearrangement of the relative amounts of ice in different categories. Rothrock's (1975) contribution was to provide a means for coupling the ice thickness distribution to the rheological behavior of sea ice. This rheological behavior, in turn, affects the ice dynamics. For this purpose Rothrock (1975) noted that the rate of work done on the ice through ridging is related to the work done by the ice interaction forces. By combining this idea with the concept of a plastic constitutive law for sea ice developed by Coon (1974), it is possible to form a coupled set of equations describing the dynamic-thermodynamic behavior of sea ice.

Numerical investigations of the variable thickness concept have mainly concentrated on examining the ice thickness distribution independent of its coupling effects on ice dynamics. Thorndike et al. (1975), for example, used the deformation field for a lagrangian parcel of ice (defined by three contemporaneous drifting stations in the Arctic Basin) together with growth rate estimates versus thickness and time to drive a thickness distribution model. Simulations with these data reproduced an ice thickness distribution in qualitative agreement with observations. Quantitative discrepancies in the results did, however, occur in the thick end of the thickness distribution. Subsequently, Maykut (1978) used observed and simulated thin ice percentages to estimate the regionally averaged heat input to the atmosphere. His estimates suggest that in the central Arctic in winter, heat exchange through ice in the 0–1.0 m thickness range is approximately equal to heat exchange through thicker ice. This is so even though the thicker ice constitutes a much larger areal fraction of the ice cover.

The simulations by Thorndike et al. (1975) and Maykut (1978) established the validity and importance of the ice thickness distribution concept. However, they were limited in the sense that changes in the ice thickness distribution were not allowed to modify the ice dynamics. In addition, a lagrangian element that covered only a small portion of the basin was used. Because of this localized lagrangian formulation, relative geographical variations were not examined and advection effects were not explicitly modeled. A useful way to examine the behavior of a variable thickness dynamic–thermodynamic sea ice model that is more fully coupled is to carry out a seasonal equilibrium simulation. Specifically, by integrating such a model over sufficiently large time intervals (several years), results for both drift and thickness can be obtained that are relatively independent of initial conditions. While a number of short-term integrations of such models have been done for localized regions (Coon et al. 1976, Pritchard et al. 1977), no equilibrium simulations have been performed. An impediment to conducting such a fully coupled dynamic–thermodynamic equilibrium simulation is the computational difficulty in solving the equations. In particular, carrying out coupled numerical simulations over times long enough to examine the thermodynamic evolution of the ice cover requires explicit inclusion of nonlinear advection terms. Such terms are not included in either the Thorndike et al. (1975) simulations or the Coon et al. (1976) and Pritchard et al. (1977) studies.

This report describes a numerical framework suitable for simulating a variable thickness sea ice cover over a seasonal cycle and presents a new redistributor for modeling ridge buildup on the geophysical scale. In addition to seasonal simulations, this model also can be applied to shorter-term forecasts. While it has certain features in common with the model developed by Hibler (1979) in an earlier study of the Arctic ice cover, the present framework contains a more general treatment of the ice strength, the ice thickness distribution, and the ice growth and decay. By combining this framework with a thermodynamic sea ice model similar to that of Semtner (1976), a seasonal equilibrium simulation of the Arctic Basin ice cover is performed. A flow chart describing the overall model is given in Figure 1.

Several shorter sensitivity studies are also carried out. In analyzing the results of these simulations, particular attention is paid to the evolution and sensitivity characteristics of the summer ice edge, and the ice thickness buildup through ridging off the Canadian Archipelago. These characteristics have not been examined in previous variable thickness studies. To a large degree this study was motivated by the lack of a variable thickness equilibrium simulation of the Arctic Basin ice cover. The main purpose of this report is to present a complete variable thickness sea ice model and to investigate the degree to which such a model with full dynamic–thermodynamic coupling can reproduce the observed thickness, drift and ridging characteristics of the Arctic Basin.
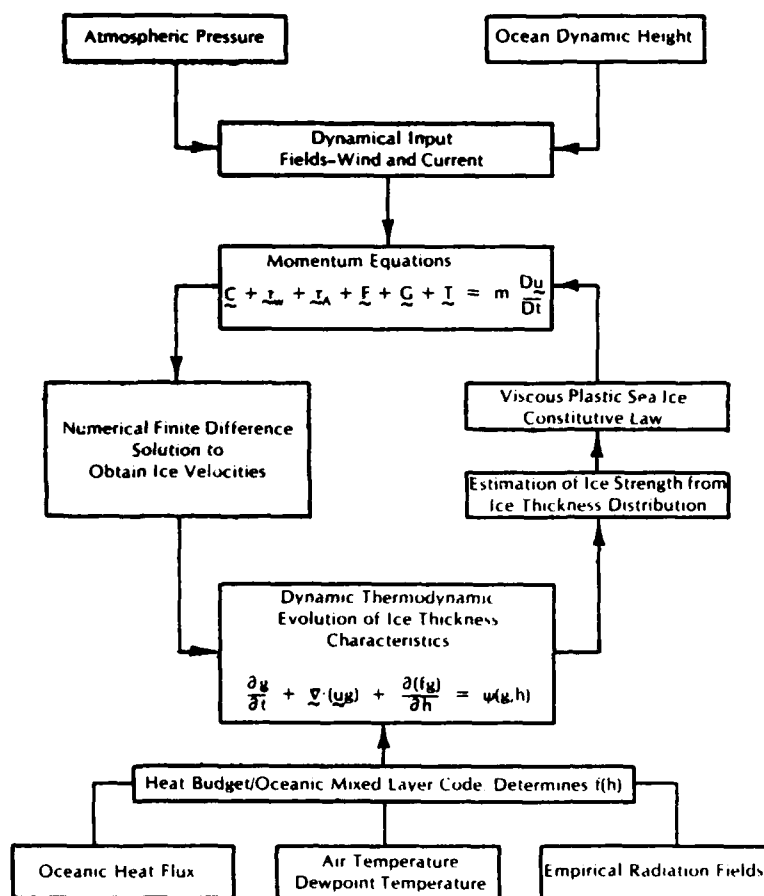
Figure 1. Flow chart for variable thickness dynamic-thermodynamic sea ice model. C—*Coriolis force;* τ_w—*water stress due to ice motion;* τ_A—*air stress;* F—internal *stress variation;* G—*ocean currents;* T—*ocean tilt;* u—*ice velocity;* D$\underset{\sim}{u}$/Dt—*ice acceleration and momentum advection;* m—*ice mass per unit area;* g—*ice thickness distribution;* f(h)—*ice growth rate;* h—*ice thickness;* ψ(g,h)—*ice thickness redistribution.*

DESCRIPTION OF THE MODEL

A fully coupled dynamic-thermodynamic sea ice model can be divided into the following components: a *momentum balance* describing ice drift, which includes air and water stresses, Coriolis force, internal ice stress, inertial forces and ocean tilt; an *ice rheology*, which relates the ice stress to the ice deformation and strength; *ice thickness distribution* equations, which describe the evolution of the ice thickness characteristics caused by thermodynamic and dynamic effects; and an *ice strength*, determined as a function of the ice thickness distribution. An additional component needed for long-term integration of the model is a *thermodynamic code*, which specifies the growth and decay rates of various ice thicknesses in the environment of a sea ice cover of variable thickness. The first two components are discussed by Hibler (1979) in a paper describing a dynamic-thermodynamic sea ice model with two thickness levels. In this model the dynamical equations include air and water stresses, Coriolis force, internal ice stress, inertial forces, momentum advection terms and ocean tilt. Nonlinear boundary layers for both the ocean-ice and air-ice surface traction are used. For the

3
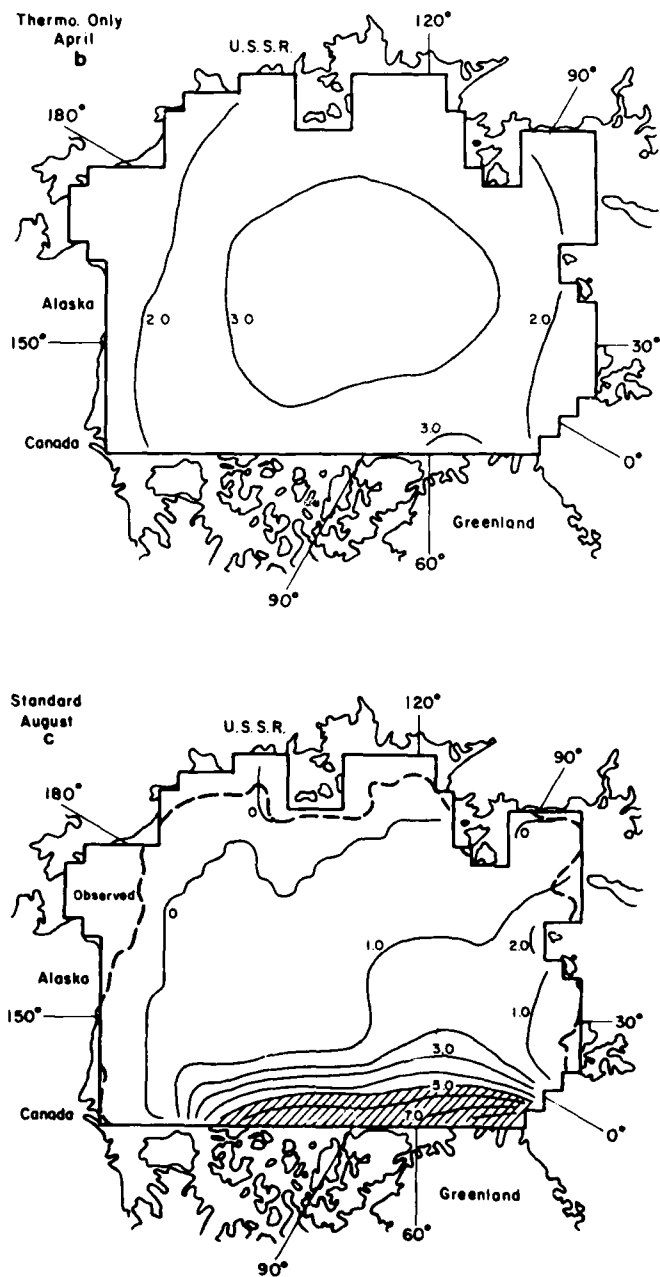
Figure 7 (cont'd).

reaches its maximum and minimum extremes in thickness and extent. For comparison the August plots show observed ice edge estimates obtained from the British Meteorological Office at Bracknell. This ice edge is the mean 40% ice concentration at the end of August over the time period 1966-1976.[*]

The dominant contrast between the two cases is a pronounced difference between the geographical variations of the ice thicknesses. The results considering only thermodynamic ef-

---

[*] Personal communication with G. Rowland, British Meteorological Office, Bracknell, England, March 1980.

A 125-km resolution grid was used for the simulations and is shown in Figure 5 (this grid is identical to that used by Hibler [1979]). Some of the numbered grid cells are referred to later in the text. The shaded grid cells near Greenland are taken to be "outflow" grid cells. Ice is only allowed to be transferred into these grid cells by advection, and once there is considered to have "flowed out" of the basin. More details on the treatment of ice dynamics and advection at such cells are given in Hibler (1979).

For the variable thickness simulations, the key results of the heat budget calculation are the ice growth rates versus thickness. Figure 6 shows the seasonal growth rates (plotted every 16 days) for different thicknesses at grid cell 8. Also plotted is the wind speed at the grid cell. The main feature is a pronounced seasonal cycle in growth rates that becomes more accentuated for thinner ice types. Superimposed on the seasonal cycle are fluctuations in growth rates attributable to variations in the sensible and latent heat losses which depend heavily on the wind speed. This heavy dependence of the thin ice and open water growth on wind speed has been experimentally observed by Andreas (1980) and is a dominant feature of Maykut's (1978) numerical heat exchange results for thin ice. Note that under summer conditions the melting rate of ice is not dependent on the thickness because of use of a fixed albedo for melting ice. However, while the total melting rate is the same, the thinner ice will have a greater ratio of bottom melt to top melt owing to the more efficient conduction of heat into the mixed layer (see Appendix B).

Basin-wide ice thickness and velocity characteristics

After 5 years both simulations approach a seasonal equilibrium, with the ice thickness and (in the standard case) ice velocity characteristics changing little between corresponding days of sequential years. The basin-wide thickness characteristics for the fifth year of integration are shown in Figure 7 for April and August. During these months the pack ice approximately
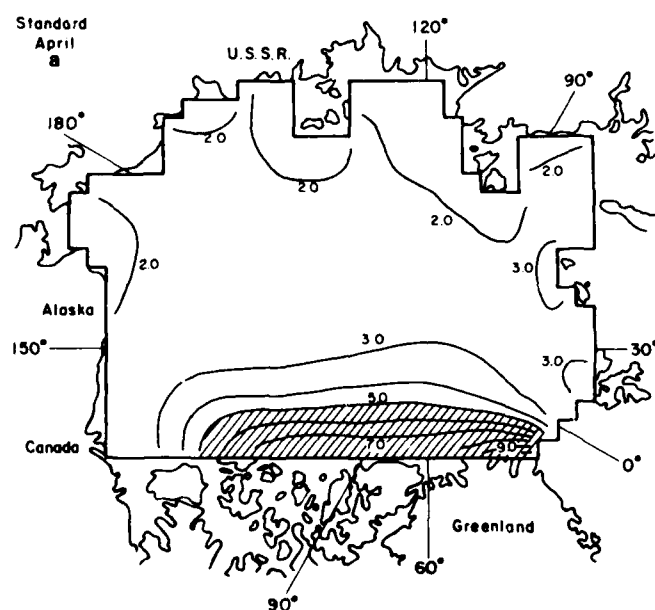
Figure 7. Average April and August thickness contours (m) for the fifth year of the standard and "thermodynamics-only" simulations. The dashed line represents the average 40% ice concentration contour at the end of August for the time period 1966-1976 as estimated by the British Meteorological Office, Bracknell, England.

16

creased to 0.66 (from 0.616 in the standard case) and the oceanic heat flux was set equal to zero. In the "strength" sensitivity study the frictional losses in ridging were taken to be nine times the potential energy change (i.e., $C = 10 C_b$ in eq 3 of Appendix A).

Input fields to drive the model consisted of monthly climatological air temperatures and dew points (from Crutcher and Meserve 1970), together with observed winds that were averaged over 8 days and varied with time over the year-long period: May 1962 to May 1963. (This particular time was chosen because of the simultaneous presence of one U.S.S.R. and two U.S. drifting ice stations that provided observed ice drift data). For the calculation of geostrophic ocean current fields, mean dynamic topography values reported by Coachman and Aagaard (1974) were used. For the radiation code, parameterizations similar to those employed by Parkinson and Washington (1979) were used. Specifically, daily global solar radiation under cloudless skies was obtained by integrating an empirical equation by Zillman (1972) over solar zenith angles for any particular day. (Zenith angles at half-hour intervals for this purpose were obtained from a numerical solution of Kepler's equation.)[*] Incoming longwave radiation was obtained using Idso and Jackson's (1969) formula for clear skies. For cloud cover estimates, values from Huschke (1969) as reported by Parkinson and Washington (1979) were employed. Readers interested in more details on the various climatological and radiation forcing fields are referred to Parkinson and Washington (1979).
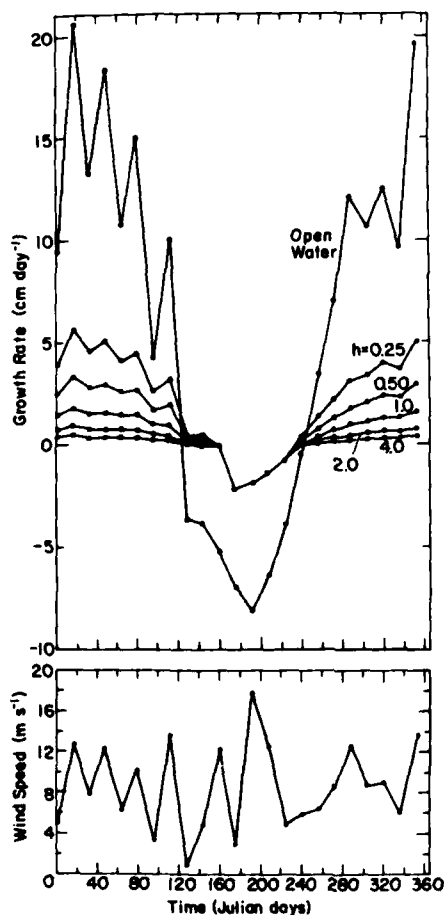
Figure 6. Growth rates versus time for different ice thickness categories at grid cell 8. Also plotted for comparison is the wind speed versus time at this location. Data points are plotted every 16 days and the ice thicknesses are labeled in metres.

---

[*] Personal communication with H. Holloway, Geophysical Fluid Dynamics Laboratory, Princeton, New Jersey, November 1979.

15
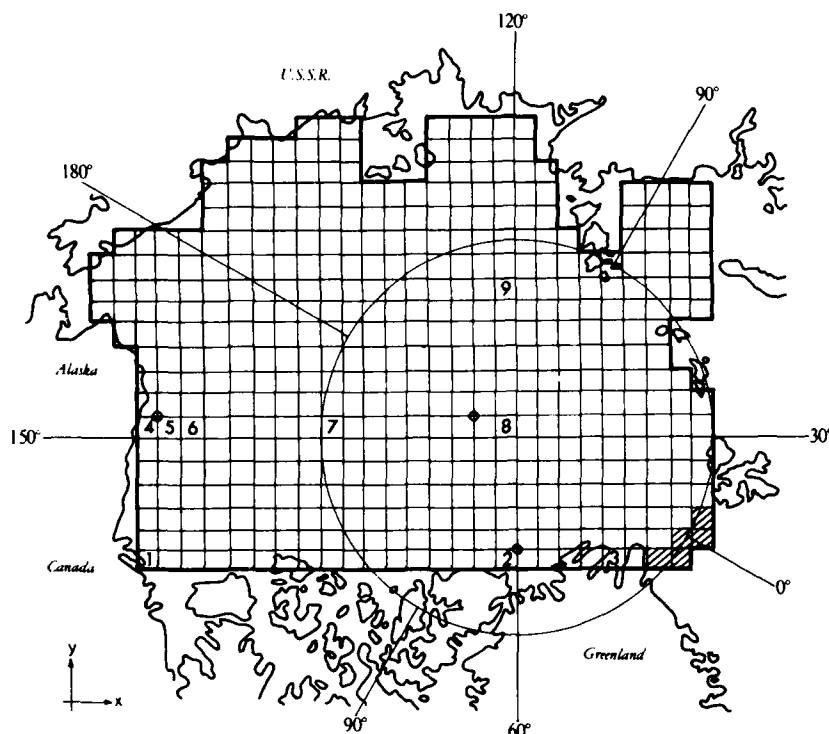
Figure 5. Fixed square-mesh grid used for numerical calculations. The numbered grid cells denote locations where time series of ice characteristics are monitored.

To investigate the behavior of this fully coupled variable thickness sea ice model, several seasonal simulations of the Arctic Basin ice cover were carried out. These simulations were performed by combining the variable thickness equations developed here, i.e., eq 4–7 and eq A5, A7, A8 and A10, with a previously developed viscous-plastic ice dynamics model (eq 1–11 of Hibler [1979]). For the standard experiment the resulting dynamic–thermodynamic system of equations was numerically integrated for 5 years at 1-day time steps using forcing fields with a 1-year periodicity. This integration time was found to be adequate to obtain seasonally varying equilibrium results. For comparison, the thermodynamic equations only were also integrated for 5 years with the same forcing. In both cases the integration was started on 1 January with mean ice thicknesses of 3.2967 m ($= 3.0 \times 10^3$ kg m$^{-3}/\varrho_i$ where ϱ_i is the density of ice) at all grid cells.

In the standard case this mean thickness was produced by including ice in the three thickness categories centered at 1.46, 2.61 and 4.23 m (see, e.g., Fig. 2). The wind and water drag coefficients and Coriolis parameter were identical to those used by Hibler (1979). The remaining constants are the mixed layer depth, d_{mix} (set at 30 m following Semtner [1976]), and various thermodynamic parameters (viz the surface albedo of ice under melting and freezing conditions, the open water albedo, the oceanic heat flux, and sensible and latent heat transfer coefficients). The values for these thermodynamic parameters for the standard case are given in Appendix B. In addition to the standard case, two shorter 1-year dynamic–thermodynamic simulations were carried out using the fourth year, 31 December, equilibrium simulation results as initial conditions. The purpose of these shorter simulations was to assess the sensitivity of the equilibrium results to ice strength and thermodynamic parameters. In the "growth" sensitivity simulation, the ice albedo under melting conditions was in-

14
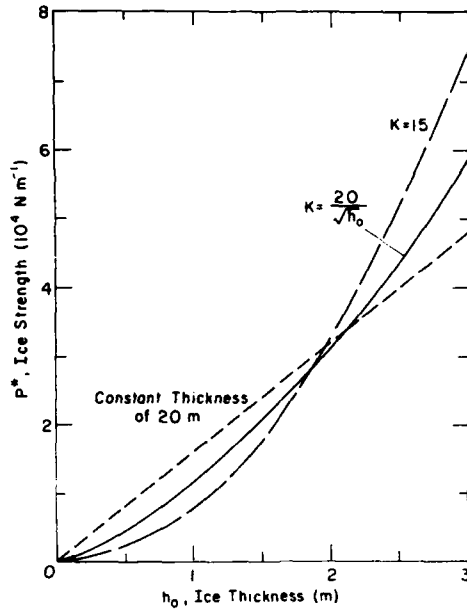
Figure 4. Ice strength versus thickness for different redistributors. The solid and long-dashed lines are for a uniform redistributor with the maximum thickness scaling as the square root (Hibler) of the thickness of ice being ridged ($K = \sqrt{h_0}$), and linearly (modified Hibler) with the thickness of ice being ridged ($K = 15$). Frictional losses are assumed to be equal to changes in gravitational potential energy.

$$P^* = \frac{Ch_0^2\,(4\Gamma^3 - 3\Gamma^2 - 1)}{3(\Gamma - 1)\Gamma}$$

where $\Gamma = \sqrt{H^*/h_0}$ for the Hibler redistributor and $\Gamma = K/2$ for the modified Hibler case,

$$P^* = Ch_0^2 K$$

(Thorndike et al.),

$$P^* = Ch_0 H'$$

(rubble redistribution). With a representative value for C of 0.8026×10^{-3} N m^{-3}, the various scalings in Figure 3 yield the strength versus thickness results shown in Figure 4. In the constant maximum cutoff case we have used the modified Hibler redistribution. However, from the above strength equation it is clear that the Thorndike et al. definition would give about the same strength versus thickness variation, but with all strengths 50% larger than the modified Hibler redistribution.

The main feature illustrated by Figure 4 is that, as expected, the square root scaling tends to give higher strengths for thinner ice than the constant scaling. The reverse is true for thick ice. However, in both these cases the three-dimensional stress will increase as the ice becomes thicker. This is in contrast to the rubble case where the three-dimensional stress will be a constant at $\approx 1.6 \times 10^4$ N m^{-2} (or ≈ 2.3 lb in.$^{-2}$).

NUMERICAL SIMULATION RESULTS

The previous section has analytically examined the character of the ridge redistribution process. However, to examine the performance of this assumed process when it is coupled to ice dynamic and thermodynamic equations, it is necessary to carry out numerical simulations.

ridge made from a single thickness of ice would have vertical sides. The Hibler redistributor avoids this feature by uniformly distributing ice from twice the block thickness up to some maximum thickness. Also, perhaps more importantly, the maximum thickness is taken to scale with the square root of the thickness of ice being ridged. This idea reflects the physical notion that for equal amounts of deformation per ridge, doubling the ice thickness will not double the maximum ridge height. This type of scaling is supported by observations (Tucker and Govoni 1981). The modified Hibler case is a uniform redistributor without this scaling. The rubble redistribution is an idealized case in which the same thickness of ice is always created.

Comparison to ridge morphological data

The scaling characteristics of different redistributors can be tested by field examination of ridge height and block size characteristics. A particularly useful data set for this purpose has been obtained and analyzed by Tucker and Govoni (1981). This data set was taken off the North Slope of Alaska. Figure 3 shows the salient characteristics of the data set that are relevant to the redistribution theory. The error bars are the standard error in the mean ridge height estimate. As can be seen from this figure, the square root scaling fits the data best.

To approximately convert the ridge height scaling to an ice thickness scaling, a 4:1 ridge keel to sail ratio is assumed (Kovacs and Mellor 1974). With this scaling the square root case is equivalent to an H^* of 100 m in the Hibler redistributor, whereas the linear scaling represents a factor of $K = 15$ in the Thorndike et al. or modified Hibler redistributors. The rubble case represents a fixed thickness $H' = 20$ m.
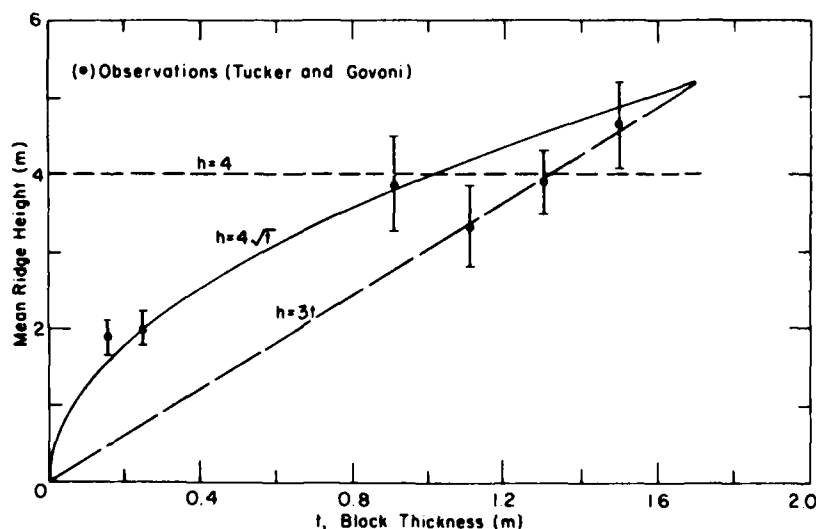
Figure 3. Comparison of different redistribution scaling laws with observed data. The solid curve represents the Hibler scaling, the long-dashed curve the Thorndike et al. or modified Hibler scaling, and the short-dashed curve the rubble scaling.

Ice strength for different redistributors

Of particular relevance to ice mechanics are the ice strengths generated by different redistributors. To get some feeling for these strengths, consider the special case of only one thickness of ice, say h_0, being ridged. Formally representing this condition by $P(h) = \delta(h - h_0)$, one can substitute eq 16 into eq 18 and obtain analytical results for the ice strength. After some algebra, different redistributors yield the following strength equations:

12

where $g(h)dh$ is the fraction of area covered by ice with thickness between h and $h + dh$. If we consider a pure convergent deformation with convergence rate $\nabla \cdot \underline{v}$, then $-\nabla \cdot v \, W_r(h,g)$ is the change in the ice thickness distribution $g(h)$ per unit time because of deformation.

In eq 16, $P(h)$ is a probability function specifying which categories are being destroyed by ridging. The quantity $\gamma(h',h)dh$ can be thought of as the area of ice put into thickness interval $(h, h + dh)$ when a unit area of ice thickness h' is used up. Basically, the integral over γ specifies where the ice is transferred during ridging by changing the areal thickness distribution function $g(h)$. It is this redistribution function γ that is of particular relevance to this paper. It can be shown (Appendix A) that to conserve mass, $\gamma(h',h)$ must obey the equation

$$\int_0^\infty \gamma(h',h) \, h \, dh = h'. \tag{17}$$

Strengths can be estimated from this kind of theory, if it is insisted that the rate of deformation work equals the work done through ridge building (Rothrock 1975). This constraint (see Appendix A) leads to the equation for the two-dimensional ice strength P^*:

$$P^* = C \int_0^\infty W_r h^2 \, dh \tag{18}$$

where the constant C

$$C = \varrho_i \frac{(\varrho_w - \varrho_i)\hat{g}}{\varrho_w}$$

is obtained by assuming the change in gravitational potential energy during ridging is equal to the frictional losses in ridging. In this expression ϱ_i and ϱ_w are ice and water densities and $\hat{g}$ is the acceleration of gravity.

Some specific redistributors

Several different forms for $\gamma(h_1,h_2)$ have been suggested. Others, although not previously suggested, are useful for pedagogical reasons. A variety of redistributors satisfying eq 17 are listed below.

$$\gamma(h_1,h_2) = \gamma(h_2 - Kh_1) \, (1/K)$$

with K = constant (Thorndike et al.),

$$\gamma(h_1,h_2) = [1/2(H^* - h_1)] \text{ for } 2h_1 \leq h_2 \leq 2\sqrt{H^*}\sqrt{h_1}$$

with H^* = constant (Hibler),

$$\gamma(h_1,h_2) = [2/h_1(K^2 - 4)] \text{ for } 2h_1 \leq h_2 \leq Kh_1$$

with K = constant (modified Hibler),

$$\gamma(h_1,h_2) = \delta(h_2 - H') \, (h_1/H')$$

(rubble redistribution).

The Thorndike et al. (1975) redistributor specifies that ice is transferred into a fixed multiple of its thickness. While this is computationally simple it has the unrealistic feature that a

11

$$\int_0^\infty gdh < 1,$$

or ridging ice if

$$\int_0^\infty gdh > 1.$$

(Note that while g is normalized at the beginning of the time step, it will not be after eq 11.) As part of this redistribution step, any negative g values (because of second order differencing in the horizontal advection equations) are set equal to zero. The net heat imbalance resulting from this removal is used to increase the mixed layer temperature to ensure that the heat budget is conserved. The final values of mixed layer temperature and g are obtained in eq 14 and 15 by laterally melting ice until either no ice is left or the mixed layer temperature is at freezing. Since any ice area lost through melting will be compensated for by increasing the open water fraction, these steps ensure that g is normalized at the end of the time step. Note that in this sequence deformation effects are included by the $\delta_x(uh)$ terms and by the open water creation. These in turn can necessitate ridging. Handling the deformation in this somewhat indirect manner allows generalization to an Eulerian grid.

ANALYTIC EXAMINATION OF THE RIDGE REDISTRIBUTION PROCESS

On the geophysical scale stresses in pack ice are largely determined by the ridge building process. To model this process on a large scale it has been suggested that thin ice be redistributed into thicker ice categories (see Appendix A). The precise manner in which this redistribution should be carried out is not clear. As an initial guess, Thorndike et al. (1975) suggested a redistribution that transfers ice into categories that are a fixed multiple of the initial thickness. Ridge observations and theoretical considerations suggest that such a redistribution is unrealistic. In order to provide a more realistic parameterization of the ridging process, a scaling law for ridge building is proposed here (see Appendix A). The purpose of this section is to examine in more detail the strength characteristics of different redistribution processes (including the particular scaling law proposed here), and to compare these processes to ridge morphological data.

Theoretical framework

In variable thickness sea ice models, the ridging process is parameterized by probability functions specifying how different ice categories are modified by deformation. Following the notation used in Appendix A, the function $W_r(h,g)$ describes this ridging process:

$$W_r(h,g) = [-P(h) g(h) + \int_0^\infty \gamma(h',h) P(h') g(h') dh'] / \int_0^\infty [P(h) g(h) -$$

$$\int_0^\infty \gamma(h',h) P(h') g(h') dh'] dh \tag{16}$$

10

the redistributor that transfers thin ice to thicker categories, and T is the boundary layer temperature. Also

$$\bar{f}(g) = \int\limits_0^\infty f(h) \, g(h) \, dh$$

$$\bar{f}_b(g) = \int\limits_0^\infty f_b(h) \, g(h) \, dh$$

$$\bar{F}_L(g,T) = \int\limits_0^\infty F_L(g,h,T) \, dh.$$

For illustration, only the x component of the ice velocity field (denoted by u) has been used and the freezing point of seawater has been set equal to zero. Also, the Du term schematically represents a horizontal diffusion term. In the complete code these diffusion terms are identical to those used in the two-level model (Hibler 1979) and were included for suppression of nonlinear instabilities. In time, u is defined at $t^{i+\frac{1}{2}}$ and the other variables in eq 8 and 9 at t^i. At the beginning of the time step it is assumed that the vertical growth rates are obtained from eq 5. To advance g and T requires the following steps (spatial and thickness differences are denoted by δ_x and δ_h, time locations by superscripts, and intermediate values within the time step by subscripts):

$$g_1^{i+1} = g^i - \Delta t \delta_x(u^{i+\frac{1}{2}} g^i) \tag{10}$$

$$g_2^{i+1} = g^i - \Delta t \{\delta_x[u^{i+\frac{1}{2}}(g^i + g_1^i)0.5] + \delta_h(f^i g^i) + Dg^i - \psi_2(u^{i+\frac{1}{2}})\} \tag{11}$$

$$T_1^{i+1} = T^i + \Delta t[\bar{f}(g^i) - \bar{f}_b(g^i)] \tag{12}$$

$$g_3^{i+1} = g_2^i + \Delta t \, \psi_1 (g_2^{i+1}, u^{i+\frac{1}{2}}) \tag{13}$$

$$g^{i+1} = g_3^i + \Delta t \, F_L(g_3^{i+1}, T_1^i) \tag{14}$$

$$T^{i+1} = T_1^i + \Delta t \, \bar{F}_L(g_3^{i+1}, T_1^i). \tag{15}$$

In this sequence eq 10 provides a provisional value of g to approximately center the spatial advection term. This approach supplies a modified Euler step (Kurihara 1965), which is second order accurate in time for the horizontal advection. After this takes place the remaining steps are basically sequential splitting steps. Equation 11 determines the change of g due to spatial advection, thickness advection and changes in open water. All advection terms are done conservatively so that all g values are conserved over the global grid. In addition, as discussed in Appendix C, the thickness advection term is done in a manner that conserves the surface heat budget components and is stable for forward time steps. In eq 12 any heat absorbed by open water that is not used in the vertical growth rates is used to increase the mixed layer temperature. In eq 13 the mechanical redistribution process is carried out (see Appendix A). This consists of normalizing g by either creating more open water if

Center of Thickness Category (m)

	0		0.26		0.71		1.46		2.61		4.23		6.39		9.10		12.39		16.24	
-0.10		0.10		0.43		1.0		1.93		3.30		5.17		7.60		10.61		14.18		18.30

Category Limits (m)

| | 0.200 | | 0.327 | | 0.573 | | 0.927 | | 1.369 | | 1.878 | | 2.430 | | 3.003 | | 3.573 | | 4.123 | |

Category Widths (m)
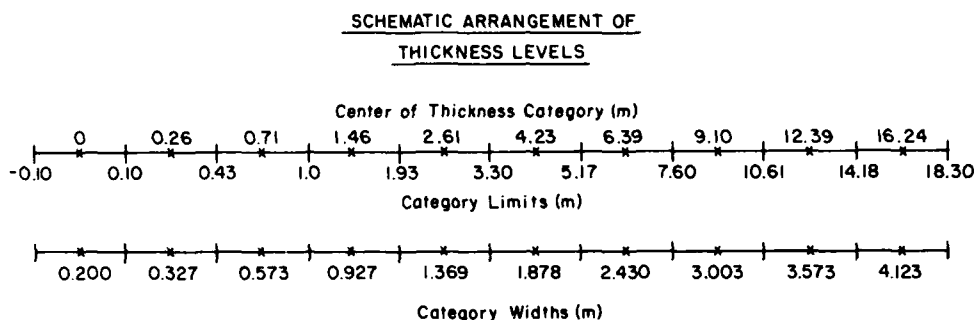
Figure 2. Schematic arrangement of thickness partition used in numerical calculations.

growth by Martin (1979) shows that growth of thin ice can be substantially enhanced by frazil ice formation. Such ice is derived from small ice crystals that form in the water column. Recent observations by Ackley et al. (1980) of the Antarctic sea ice field indicate that the frazil ice component of Weddell Sea pack ice is substantially larger than that found in the Arctic. As a consequence, inclusion of enhanced thin ice growth may be important for Antarctic pack ice simulations.

Numerical scheme

Equations 4–7 are numerically solved as an initial value problem using finite difference techniques. While the strengths are generated differently, the numerical coupling of these equations with the dynamics proceeds in the same way as employed previously for a coupled two-level model (Hibler 1979). Since the numerical scheme for the two-level model is discussed by Hibler (1979), it is enough here to present the time marching scheme and finite differences used to solve eq 4–7. The time marching scheme is briefly sketched below. Details on the thickness partition and finite difference code are given in Appendix C. In general the numerical complexity of the equations is substantially increased by the inclusion of the advection terms. These advection terms arise because fixed grids in both space and thickness are used. The spatial grid is a regular mesh staggered configuration (see Fig. 5, Hibler 1979) with thickness characteristics defined at the center and velocity points defined at the corners. The thickness grid is composed of an arbitrary number of irregularly spaced thickness levels. For the simulations performed here, ten thickness levels are employed as shown in Figure 2. In this grid larger categories are used for thicker ice since growth rates change less rapidly there. Open water is considered simply by having one thickness category centered at zero thickness. These thickness levels remain fixed. However, the relative areal extent of the ice in each category evolves in response to vertical ice growth, spatial advection, deformation and lateral melting.

To solve eq 4–7 a series of splitting operations is used. In a fixed Eulerian grid, the sequence in which these operations are performed is critical since it is important that certain operations be done last to ensure conservation of several quantities. The time marching scheme for the coupled thickness equations can be illustrated using the following simplified equations:

$$(\partial/\partial t) = -(\partial/\partial x)(ug) - (\partial/\partial h)(fg) + F_L(g,T) + \psi_1(g,u) + \psi_2(u) - Du \qquad (8)$$

$$(\partial T/\partial t) = \bar{F}_L(g,T) + [\bar{f}(g) - \bar{f}_b(g)] \qquad (9)$$

where ψ_2 is the portion of the redistributor that only creates open water, ψ_1 is the portion of

8

tion to the amounts of heat absorbed by leads and not used in increasing the rate of vertical melt. Equation 7, on the other hand, states that there will be enough instantaneous lateral melt to either lower the mixed layer temperature to freezing or to remove all the ice. Also, eq 7 assumes that lateral melt reduces all ice thicknesses by the same percentage. The physical argument here is that ice will lose mass by lateral melting in proportion to its thickness. This, in turn, is based on the physical notion that thicker ice will have a larger vertical interface with the ocean than thinner ice. Coupling the equations in this way removes the necessity of considering any special cases. For example, cooling off a warm, ice-free mixed layer is naturally treated in eq 5–7 by simultaneously freezing ice and removing the frozen ice by lateral melting.

While better parameterizations are needed, numerical experiments with this mixed layer growth model, coupled to the variable ice thickness model discussed earlier, can help determine the relative role of dynamics and thermodynamics in sea ice growth, drift and decay. The idea in the (0) ≥0 case is that under "winter conditions" the growth rates of the sea ice cover are basically vertical and are dominated by heat budget considerations. This assumption is reasonable in the Arctic Basin, where leads do not long remain ice-free, and is consistent with sensitivity studies by Maykut (1978). The heat budget code described here approximates these features. The main shortcoming is that the effect of snow cover on the conductivity of the snow–ice system is not included. While this feature is not critical to equilibrium thicknesses (see, e.g., Maykut and Untersteiner 1971), snow does substantially affect the growth rates of thin ice (Maykut 1978). Improvements of this parameterization are needed. However, it should be noted that in a coupled model inadequate estimates of thin ice growth rates may well be offset by larger thin ice growth estimates shortening the thin ice lifetime. Consequently, time-averaged energy exchange may not be critically affected.

Under melting conditions the open water heat absorption terms reflect the fact that boundary layer warming and lateral melting can substantially affect the decay of sea ice. Effects of this kind have been discussed in reviews by Rothrock (1979), Wadhams (1980) and Hibler (1980b). Lateral melting has been particularly emphasized by Zubov (1945) and Langleben (1972) in studies of shore-fast ice decay. These authors have explained observation of shore-fast ice decay by using absorbed radiation solely in decreasing the horizontal dimensions of floes. Wadhams (1980) has suggested that near the ice edge, lateral melting may depend upon the geometric properties of the ice. Specifically, as floes become smaller and more numerous, the effective "length" of flow edges increases. In addition to lateral melting, the movement of the ice and the wind mixing will cause the ice to move over regions that were formerly leads. Summer observations of the mixed layer and ice drift by McPhee (1980b) indicate that substantial vertical mixing can be induced by the wind and ice motion. Also, near the ice edge turbulence and wave effects can cause horizontal mixing and enhance vertical melt (see, e.g., Wadhams et al. 1979). The parameterization suggested here approximates these processes primarily by increasing vertical melting due to heat absorption. In addition, for a sufficiently loose pack, lateral melting terms are added.

In both the decay and growth cases a possible modification would be to allow different growth and decay rates for thick ice. Very thick ice in the form of ridges may well behave differently than level ice. Ablation observations by Koerner (1973), for example, indicate that the upper surfaces of first-year ridges ablate much more rapidly than level ice. Such effects may be even more pronounced on the bottoms of ridges, where the deep keel of a ridge allows ablation at the sides as well as on the bottom of the ice. In light of these considerations some type of parameterization of the growth rates as a function of the geometric properties of pack ice is needed.

Finally, in the growth case it is possible that thin ice growth rates may be substantially larger than those based on heat budget considerations. Specifically, analysis of young ice

7

Under conditions where open water is losing heat to the atmosphere, the heat budget growth rates [denoted by $f_b(h)$] are taken to be the vertical growth rates in eq 4. However, when open water is absorbing heat, the heat is allowed to mix underneath the ice flow and decrease the vertical growth rate of all categories down to some minimum value. Any remaining heat is allowed to either cause lateral melting or raise the temperature of the mixed layer. In this specific parameterization the mixed layer temperature is always kept at freezing in the presence of an ice cover. Consequently, all available heat absorbed by leads and not used in vertical melting is used in lateral melting until the ice disappears. Also, under growth conditions no ice is allowed to form until the mixed layer reaches the freezing temperatures of seawater.

The vertical rates in this parameterization may be formally described by

$$f(h) = \begin{cases} \text{Max}[0, f_b(0)] & \text{if } h = 0 \\ \text{Max}\left\{f_1, \left[f_b(h) + \dfrac{(1-g_i)}{g_i} \text{Min}(f_b(0),0)\right]\right\} & \text{if } h > 0 \end{cases} \tag{5}$$

where g_i is the fraction of area covered by ice, which is defined as

$$g_i = \lim_{\epsilon \to 0} \int_\epsilon^\infty g(h)dh.$$

Specifying a minimum decay rate, f_1, is based on the physical notion that there is a limit to how rapidly sea ice may melt in water near the freezing point. In the simulation performed here, f_1 is taken to be –15 cm/day. This number is close to the maximum wave-induced melting rates calculated by Wadhams et al. (1979).

The lateral melting and warming of the mixed layer are described by the coupled equations

$$\frac{\partial T_{mix}}{\partial t} = 271.2 + [Q_i/(C_v d_{mix})]\left\{\int_0^\infty F_L(g,h,T_{mix})hdh + \int_0^\infty [f(h)-f_b(h)]g(h)dh\right\} \tag{6}$$

$$F_L(h,g,T_{mix}) = \begin{cases} -C(T_{mix})g(h) & \text{for } h > 0 \\ C(T_{mix})g_i\delta(h) & \text{for } h = 0 \end{cases} \tag{7}$$

where

$$C(T_{mix}) = \text{Min}\left\{\frac{(T_{mix}-271.2)}{Q_i \bar{h}} C_v d_{mix}, 1\right\}$$

with $\bar{h}$ the mean ice thickness

$$\bar{h} = \int_0^\infty g(h)hdh.$$

In these equations T_{mix} is the mixed 'ayer temperature in Kelvins, d_{mix} is the mixed layer depth, Q_i is the volumetric heat of fusion of ice (set at 302 MJ m^{-3}), and C_v is the volumetric heat capacity of water (set at 4.19 MJ m^{-3}). Also, in eq 6 and 7 the freezing temperature of seawater is taken to be 271.2 K. Equation 6 specifies that the mixed layer temperature will decrease in proportion to the mass of ice removed by lateral melting and increase in propor-

6

causes the more general thickness distribution equation to become

$$\frac{\partial g}{\partial t} + \nabla \cdot (\underline{u} g) + \frac{\partial (fg)}{\partial h} = F_L + \psi. \tag{4}$$

Considerable complexity in the equation resides in the mechanical redistribution function ψ. Because of this complexity a more complete discussion of ψ is given in Appendix A. There, a specific redistribution function is proposed and the relation of the ice strength to the ice thickness distribution is briefly discussed. In addition, because of the importance of ridging, the ramifications of the ridge distribution process proposed in Appendix A are analytically examined and compared to observed data in a later section. However, for the present discussion it is enough to note that ψ creates open water under pure divergence and transfers thin ice to thick ice categories under pure convergence. For an arbitrary deformation state, the open water creation and ridging are considered to be simultaneous. In addition the strength of the system is related to the amount of thin ice, so that thicker, more compact ice will exhibit greater strength and, hence, greater resistance to compression.

Heat budget and oceanic boundary layer

Given vertical and lateral growth rates, one could use the thickness distribution (eq 4) to determine the evolution of g. However, to determine these growth rates is a complex task and it minimally requires consideration of the oceanic boundary layer and heat budget at the air/sea ice interface. For this purpose a simple parameterization consistent with available knowledge is suggested here. Some of the complexity that might be considered in a more detailed parameterization is discussed later in this section.

Basically, at each ice thickness category vertical growth rates are estimated 1) from heat budget considerations at the top and bottom surface of the ice and 2) by adding, via lateral mixing, some of the heat absorbed by leads. In the heat budget calculations a simple time-independent thermodynamic sea ice model is used. Following Semtner (1976), this model approximates the heat transfer through the ice by assuming a linear temperature profile together with a constant ice conductivity. However, in contrast to Semtner (1976), the conductivity effects of a snow cover are not considered. Instead, following Bryan et al. (1975) and Manabe et al. (1979) the model approximates the effects of snow cover by allowing the ice surface albedo to be that of snow when the calculated surface temperature is below freezing and that of snow-free ice when the surface temperature is at the melting point. With these assumptions the upward heat flux (I_H) through ice of thickness H is

$$I_H = (K/H) (T_w - T_o)$$

where K is the ice conductivity, T_w the water temperature and T_o the surface temperature of the ice. This simple thermodynamic model is used in conjunction with a surface heat budget computation similar to that of Parkinson and Washington (1979) and Manabe et al. (1979). In this computation (see Appendix A) the surface temperature of the ice that balances the surface heat budget is obtained by iteration. This temperature then dictates the conduction of heat through the ice and, hence, the ice growth rate. If the iteration yields an above-freezing value, the surface temperature is set at the freezing point. Surface and bottom ablation rates are then determined by imbalances in the surface heat budget and by the conduction of heat into the mixed layer. As in Maykut and Untersteiner (1971), the effect of heat transfer from deep, warmer ocean water is approximated by assuming a constant oceanic heat flux into the mixed layer. This thermodynamic model and surface heat budget computation is described in more detail in Appendix B.

5

ice rheology a viscous plastic constitutive law is used. Rigid plastic behavior is approximated in this law by allowing the ice to flow plastically for normal strain rates and to creep in a linear viscous manner for small strain rates. Documentation of this dynamical code is available (Hibler 1980a).

In the work presented here, the dynamical formulation used by Hibler (1979) is employed. However, a more general treatment of the ice thickness distribution, the ice strength and the thermodynamic code is presented.

Ice thickness equations

For the purposes of this paper the ice is considered to be a two-dimensional continuum with a velocity field u. This velocity field is obtained by solving a momentum balance (see Hibler 1979) that includes the effects of internal ice stress. The stress state in the ice is described by a plastic constitutive law

$$\sigma_{ij} = \sigma_{ij}(\epsilon_{ij}, P^*) \tag{1}$$

where σ_{ij} is the two-dimensional stress tensor, ϵ_{ij} the strain rate tensor and P^* the ice strength. As discussed in more detail in Appendix A, P^* is a function of the amount of thin ice present in the ice cover.

As in Thorndike et al. (1975), the ice thickness characteristics are described by an areal ice thickness distribution $g(h, \underline{x}, t)$ where $g(h, \underline{x}, t)dh$ is the fraction of area (in a region centered at position $\underline{x}$ at time t) covered by ice with thickness between h and $h + dh$. This distribution evolves in response to deformation, advection, growth and decay. Neglecting lateral melting effects, Thorndike et al. (1975) derived the following governing equation for the thickness distribution:

$$\frac{\partial g}{\partial t} + \nabla \cdot (\underline{u}g) + \frac{\partial (fg)}{\partial h} = \psi \tag{2}$$

where f is the vertical growth (or decay) rate of ice of thickness h and ψ is a redistribution function (depending on h and g) that describes the creation of open water and the transfer of ice from one thickness to another by rafting and ridging. In general, f is a function of $g(h)$, and ψ is a function of both $g(h)$ and the rate of deformation. Except for the last two terms, eq 2 is a normal continuity equation for g. The last term on the left-hand side can also be considered a continuity requirement in thickness space since it represents a transfer of ice from one thickness category to another by the growth rates. An important feature of the Thorndike et al. (1975) theory is that it presents an "Eulerian" description in thickness space. In particular, growth takes place by rearrangement of the relative areal magnitudes of different thickness categories.

Equation 2 can be formally generalized to include lateral growth by simply adding a source and sink term $F_L(g, h)$ such that

$$\int_0^\infty F_L \, dh = 0. \tag{3}$$

Equation 3 follows from the fact that, by definition, lateral melting (or freezing) of ice will be compensated for by a change in the extent of open water. In addition $F_L > 0$ for $h = 0$ and $F_L < 0$ for $h > 0$. These conditions reflect lateral melting decreasing the areal extent of ice while increasing the open water extent. The addition of this lateral growth term to eq 2
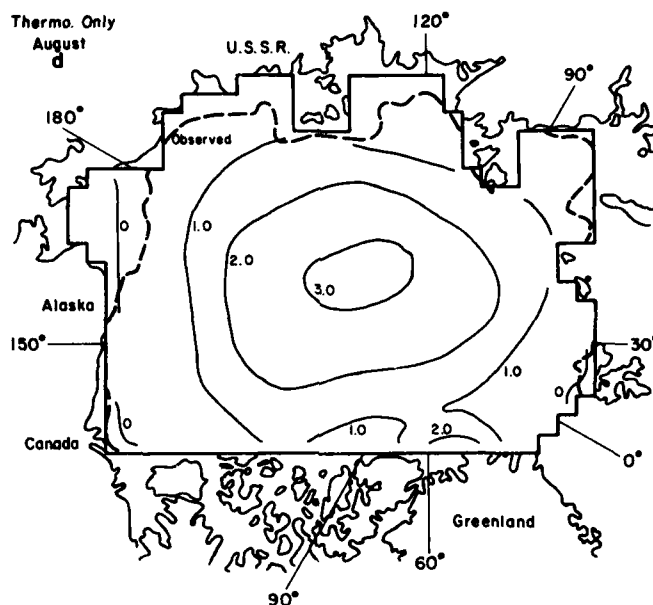
4

Figure 7 (cont'd). Average April and August thickness contours (m) for the fifth year of the standard and "thermodynamics-only" simulations. The dashed line represents the average 40% ice concentration contour at the end of August for the time period 1966-1976 as estimated by the British Meteorological Office, Bracknell, England.

fects are very similar to those obtained by Washington et al. (1976), with ice exceeding 3 m in the central basin in winter, and all the ice at certain near-shore locations melting in summer. The standard case, on the other hand, exhibits a pronounced ice buildup along the Canadian Archipelago. The reason for the spatial variation in the standard case is apparent from examination of the annual ice velocity field in Figure 8. This field exhibits a clockwise Beaufort Gyre and transpolar drift in agreement with observations of the mean annual drift (see, e.g., Gordienko 1958). While instantaneous velocities may differ substantially, on the average the drift tends to thin the ice off the Alaskan and Siberian coasts while increasing the ice thickness off the Canadian Archipelago. The shape and magnitude of the standard case ice thickness contours agree well with observed estimates. Figure 9, for example, shows observed results based on submarine data, portions of which are reported by LeShack et al. (1971). Similar spatial thickness variations have been obtained from airborne and subsurface studies of the ridge statistics in the Arctic Basin (see, e.g., Hibler et al. [1974] and Wadhams [1981]).

The summer ice edge characteristics of the standard case are, however, less realistic. Specifically, while the shape of the ice edge is reasonable, its location is consistently too far from shore. It also appears that the standard case is yielding rather large amounts of open water in the central basin. This feature is demonstrated in Figure 10, which shows mid-month compactness transects from July through October. These transects were taken along a line connecting grid cells 4 and 8 (see Fig. 5). Using a large amount of data from aerial reconnaissance flights, Wittmann and Schule (1966) have estimated that from August to October there is typically about 12% open water in the Canadian Basin (between the Pole and Alaska), and 7% in the Eurasian Basin (between the Pole and Franz Josef Land). The August through October averages of the simulated values agree with the geographical trend of these observations, but are somewhat larger. However, the substantial month-to-month variations in the

18
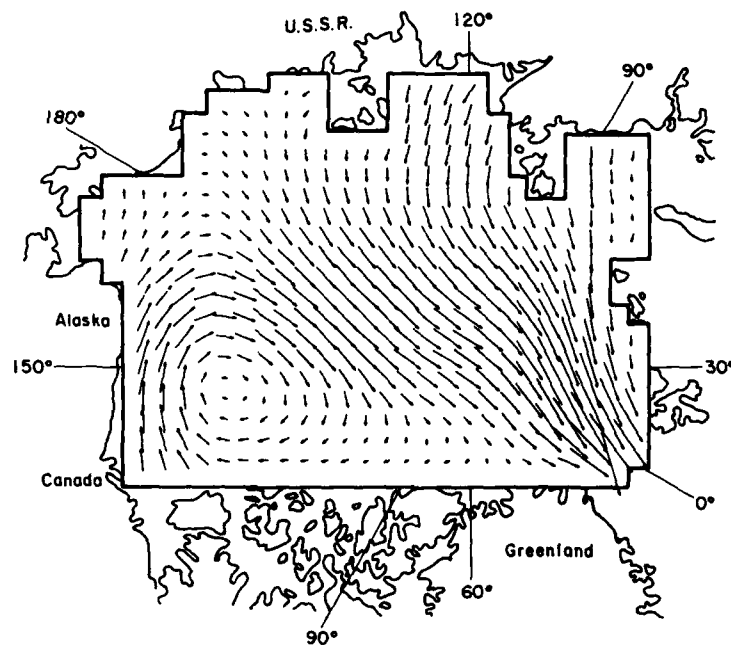
Figure 8. Average annual ice velocity field for the fifth year of the standard simulation. A velocity vector of one grid space long represents 0.02 m s⁻¹.
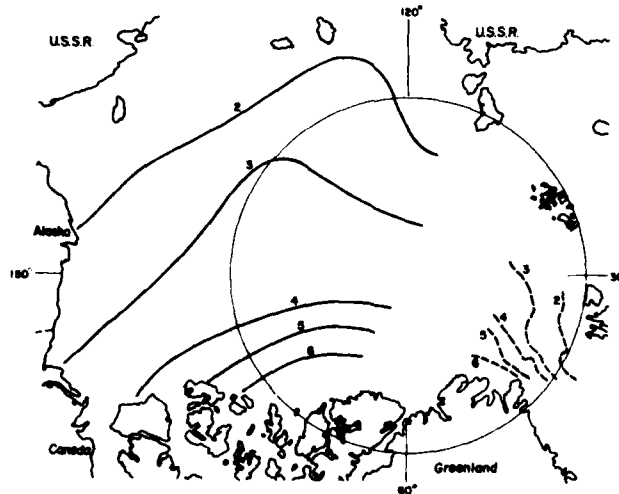
Figure 9. Approximate contours (m) of observed ice thickness values obtained from submarine sonar data (personal communication with L.A. LeShack, LeShack Associates, Silver Spring, Maryland, 1979). The solid contours were obtained by LeShack from a composite analysis of both summer (1960, 1962) and winter (1960) data, whereas the dashed contours are from April 1977 data.
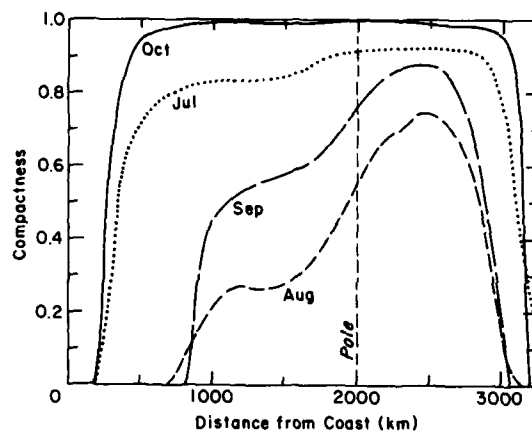
19

Figure 10. Mid-month ice compactness transects for the fifth year of the standard simulation. These transects were taken along a line connecting grid cells 4 and 8.
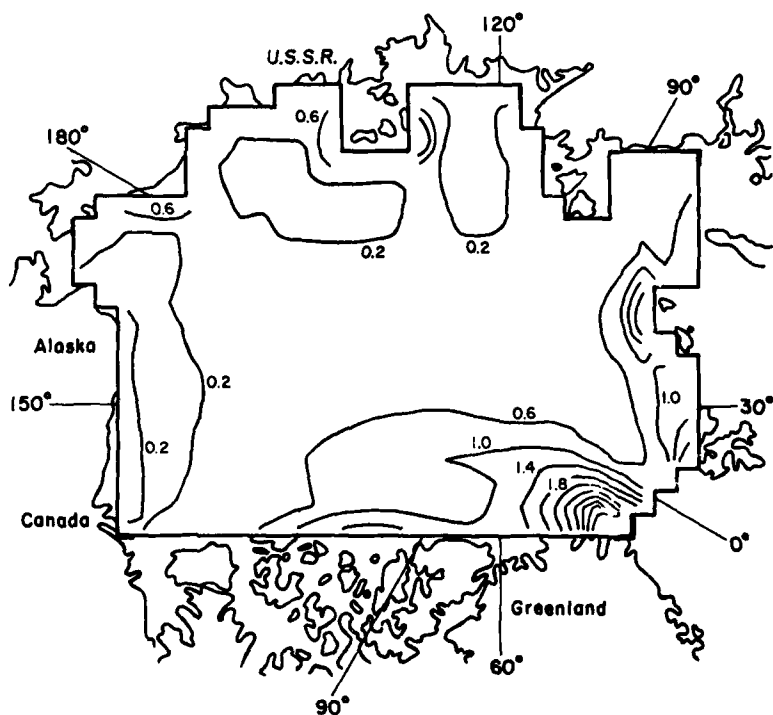

Figure 11. Contours (m) of simulated volume of deformed ice per unit area for one annual cycle.

20

simulated compactness values (see Fig. 10) indicate that real time observations are needed for detailed verification. Similar considerations also apply to ice edge variations, since year-to-year values of the ice edge can differ significantly from climatological means (see, e.g., Walsh and Johnson 1979b).

Of particular interest to this author are the ridge buildup results. While the model does not explicitly keep track of ridging, it is possible to determine the volume of deformed ice created over an annual cycle at a fixed location. Figure 11 shows contours of this quantity. The general shape of the roughness contours agrees well with surface roughness observations in the western Arctic Basin (Weeks et al. 1971, Hibler et al. 1974). The two major features are a heavy buildup of ridging off the Canadian Archipelago and less ridging in the Beaufort Sea than near the Pole. Note, however, that there is a zone of heavy ridging just off the North Slope, in agreement with observations by Tucker et al. (1979). The other major feature is a tongue of high ridging further offshore near the tip of Greenland. Roughness data obtained from submarine sonar profiles by LeShack* also show such a tongue.

Ice edge evolution and sensitivity

The ice edge characteristics take several years to fully evolve. This evolution time is illustrated in Figure 12, which shows the mid-September ice thicknesses along a transect perpendicular to the North Slope. As is apparent, the ice edge takes about 3 years to completely develop, with the difference between the first two summers being most pronounced. Because of this long evolution time, it is possible that some of the unrealistic results may be attributable to the choice of the wind field for a particular year. By considering interannual variability in a simulation, earlier years with, say, less persistent offshore winds in summer could reduce the formation of an excessive ice edge in a particular year.
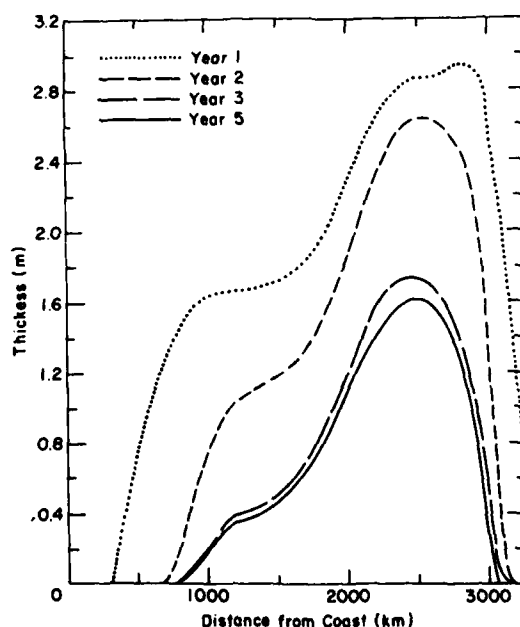
Figure 12. Evolution of the mid-September (day 257) ice thickness characteristics in the standard simulation. Thickness transects along a line connecting grid cells 4 and 8 are plotted.

---

* Personal communication with L.A. LeShack, LeShack Associates, Silver Springs, Maryland, 1979.

21
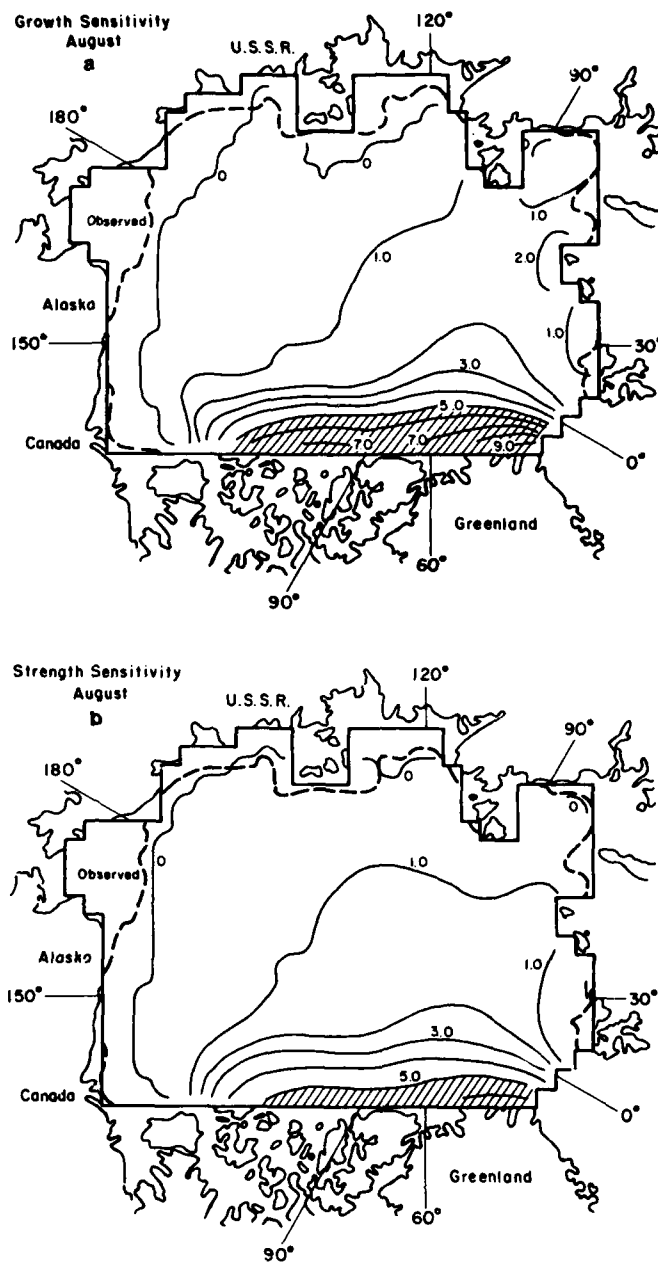
*Figure 13. Average August thickness contours (m) for the
high-strength and high-growth simulations.*

However, while the interannual variability may be a factor, it seems likely that the unrealistic ice edge is primarily caused by inadequate tuning of the dynamic and thermodynamic parameters. This possibility is supported by the 1-year sensitivity studies. The improvement yielded by these simulations is illustrated in Figure 13, which shows August thickness contours, and Figure 14, which shows mid-August compactness transects. The initial conditions for these simulations were the 31 December data from the fourth year of the standard simulation. Consequently, the different ice edge characteristics only have about 8 months to

22
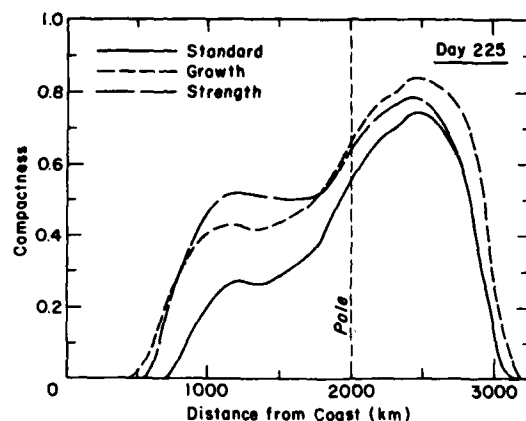
Figure 14. Mid-August compactness transects (through grid cells 4 and 8) for the standard and two sensitivity simulations.

evolve. Even over this short time there is a significant improvement in both the ice edge location and the amount of open water formed in the central Arctic. Note also that both sensitivity simulations yield a sharper ice edge with a rapid rise to about 40% ice concentration.

While the increase in ice stress in the "strength" study is probably excessive, the change in parameters for the "growth" simulation is within the range of uncertainty of the forcing parameters. The ice albedo under melting conditions for the high-growth case, for example, is equal to Semtner's (1976) adjusted value for multiyear ice. While this value may be a bit high for ice covered with melt ponds (see, e.g., Langleben 1971), summer radiation values are not known precisely because of, for example, uncertainties in cloud cover. Also, adding in increased ice growth rates from snowfall could largely offset the oceanic heat flux term in the simple thermodynamic ice model used here.

Analysis of these sensitivity results shows that the reasons for the improvement of the ice edge are quite different for the two sensitivity simulations. In the case of the thermodynamic sensitivity study, it is mainly a case of reduced summer melting, which simply melts less ice. In the dynamics case the effect is primarily one of reducing offshore advection, especially at a critical time in the early spring. The advection effect is illustrated in Figure 15a, which shows the difference between ice growth and actual ice thickness at grid cell 4. A major difference between the simulations occurs in the spring at approximately day 120. At this time both the high-growth simulations show a sharp reduction in thickness owing to the dynamics, whereas the high-strength case does not. Examination of the high-strength case shows that the basin is practically frozen by the high ice stresses in early spring, thus preventing such offshore motion. This lack of offshore motion in turn keeps the ice from thinning early in the melt season and, hence, reduces the amount of offshore open water. While such motionless situations are unrealistic for this year (see the next section), they do occur under certain onshore or quiescent wind conditions as documented by Thorndike and Colony (1980) for the Beaufort Sea.

The role of reduced summer melt for the high growth case is illustrated in Figure 15b, which compares ice thicknesses versus time at grid cell 6. This figure also demonstrates the importance of the boundary layer heat storage on fall ice freezeup. Since the open water albedo has not been changed, this reduced summer melt is primarily caused by reduced ice melt. (A smaller portion of the reduction is attributable to setting the oceanic flux term equal to zero.) On the basis of this sensitivity study it seems likely that inclusion of a snow cover

23
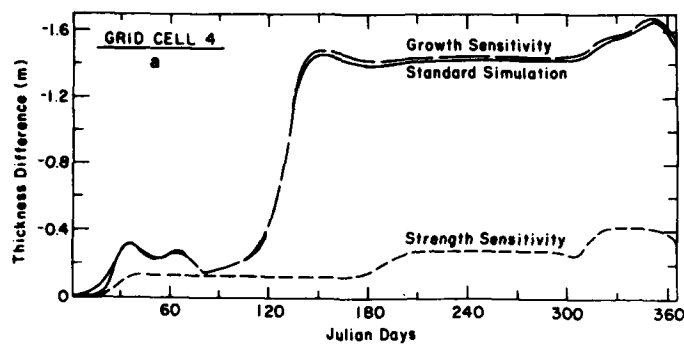
a. Ice thickness and the net ice growth at grid cell 4.
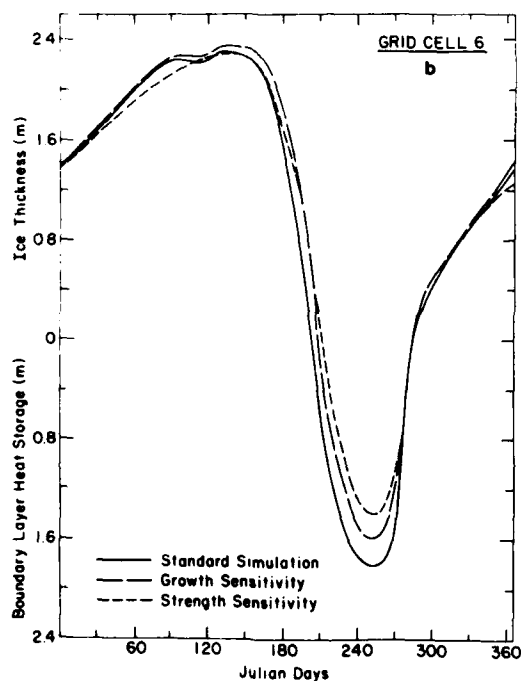
b. Ice thickness and boundary layer heat storage (in equivalent ice thickness units) at grid cell 6.

Figure 15. Time series of the difference between parameters.

would improve the simulated ice edge. With a snow cover it might take several weeks to melt the snow and reduce the surface albedo to snow-free values. In the simplified model used here, the surface albedo changes immediately after melting conditions commence.

It is also likely that some of the excessive summer melt in the standard case is caused by an unrealistically small albedo of open water (0.1). Observational estimates (Langleben 1971) are closer to 0.2, a value that is commensurate with albedos in the polar regions used in most climate models (see, e.g., Manabe and Stouffer 1980).

24

It is possible that these sensitivity results may have relevance to ice edge forecasting. Rogers (1978), for example, has found the air temperature, in the form of thawing degree days, is the parameter that correlates most highly with the summertime ice margin off the North Slope. Barnett (1980), on the other hand, has found that pressure changes in April correlate well with a combined severity index of North Slope ice conditions in August and September. The simulation done here suggests that, while thermodynamics probably controls the overall degree of melt, dynamical effects early in the spring may be critical in thinning out the near-shore ice. This thinning can then produce a local ice edge even under relatively "cool" conditions.

Ice thickness characteristics off the Canadian Archipelago

The ice thickness characteristics off the Canadian Archipelago also require several years to fully evolve. However, this evolution is one of thickness buildup rather than decay. Some of the evolution characteristics are illustrated in Figure 16, which shows the ice thickness and fraction of thick ice on a transect between grid cells 2 and 8. Also shown in this figure is the total amount of ice ridged per year. The observed data were taken from submarine sonar estimates of ice thickness and the thick ice fraction obtained by Wadhams (1981) using October 1976 data from the HMS *Sovereign*.

The main characteristic of the evolution is a gradual increase in ice thickness near the coast, coupled with a decrease at the Pole. The slow buildup comes from to new thin ice being ridged each year, thus gradually increasing the thickness. The thinning of ice near the Pole, on the other hand, appears to be primarily an advection process, with thinner ice from the Beaufort Sea being brought in. The 2-year lag is needed for this thinning because the ice in the Beaufort Sea is rather thick at first because of the initial conditions. This decrease in thickness is also accompanied by a more peaked and less asymmetric thickness distribution at the Pole on year 5 than on year 2. This characteristic is illustrated in Figure 17, which shows the interannual evolution of the simulated ice thickness distribution near the Pole. For a comparison to observations, Figure 17 also shows observed ice drift distributions near the
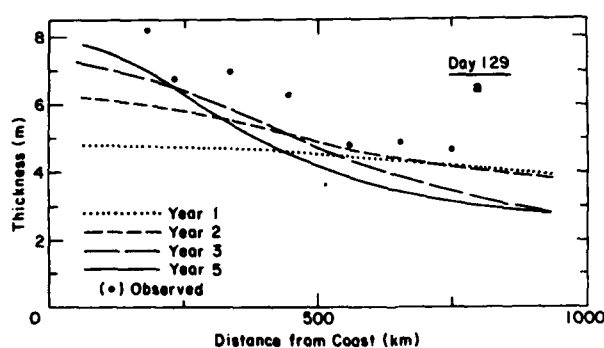
a. Ice thickness.

Figure 16. Evolution of the simulated ice thickness characteristics off the Canadian Archipelago along a transect through grid cells 2 and 8. The observed thickness results were obtained in (a) by multiplying ice draft data from Wadhams (1981) by 1.1 to approximately convert ice drafts to thickness and in (b) by using Wadham's areal percentages for ice drafts deeper than 5 m.

25
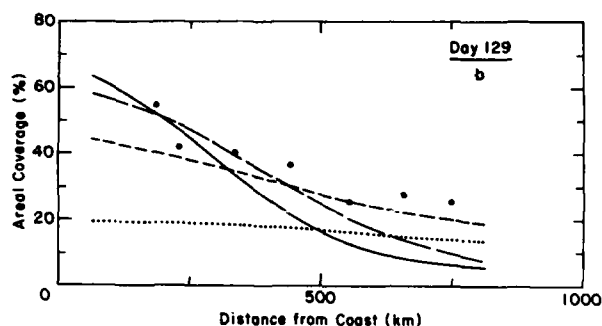
b. Fraction of area covered by ice thicker than 5.17 m.
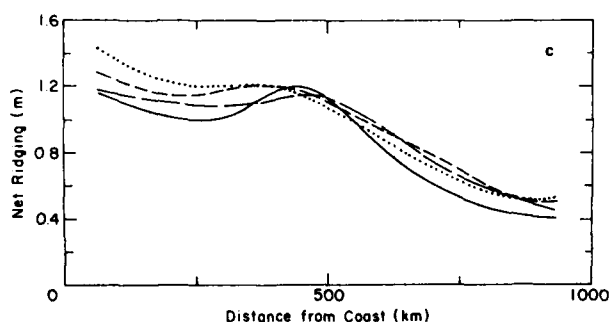
c. Net ice ridged (in metres) over an annual cycle.

Figure 16 (cont'd). Evolution of the simulated ice thickness characteristics off the Canadian Archipelago along a transect through grid cells 2 and 8. The observed thickness results were obtained in (a) by multiplying ice draft data from Wadhams (1981) by 1.1 to approximately convert ice drafts to thickness and in (b) by using Wadham's areal percentages for ice drafts deeper than 5 m.

Pole obtained by Wadhams (1981) and by LeShack.* The LeShack data were obtained from the February 1960 cruise of the USS *Sargo*.

Figures 16 and 17 show the simulated results to have a thick ice percentage similar to Wadhams's data, but somewhat smaller thickness values, especially near the Pole. Part of this discrepancy may arise from insufficient growth. In the growth sensitivity study, for example, there is a considerable increase in thickness after only 1 year. This feature is shown in Figure 18, which compares sensitivity transects off the Canadian Archipelago with the standard case. However, there may also be significant amounts of interannual variability. The LeShack data at the Pole, for example, are in better agreement with the simulated values than Wadhams's data.

An interesting feature shown by the net ridging is a slow evolution of a zone of high ridging several hundred kilometres off the coast. This feature does not occur the first few years, which indicates that it is probably related to the spatial variations in ice strength that are gradually built up. While this ridging peak is not manifested in the simulated thick ice per-

---
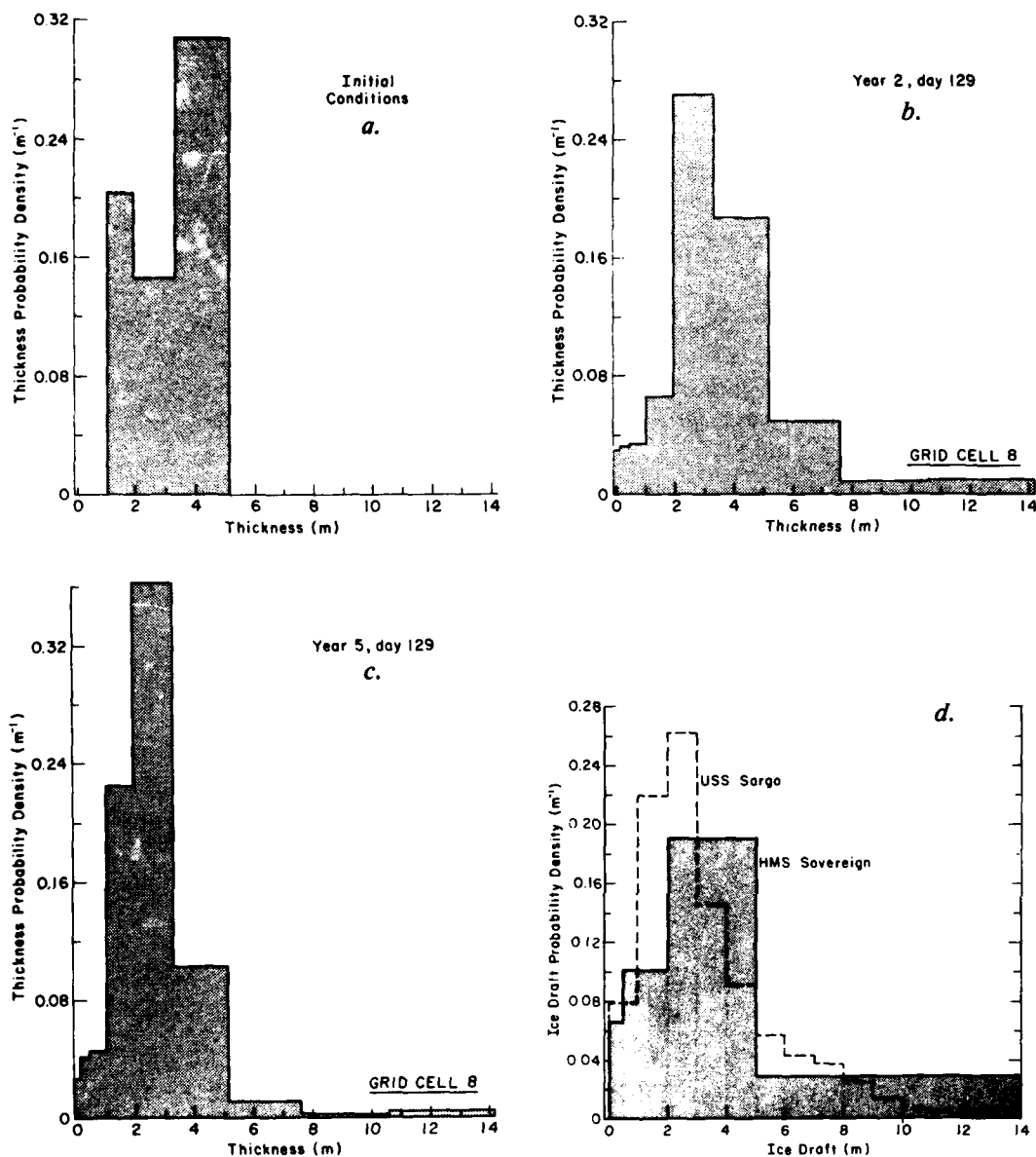
Figure 17. Interannual evolution of the simulated ice thickness distribution at the Pole (grid cell 8). The observed ice draft distributions were obtained by Wadhams (1981) using October 1976 HMS Sovereign *data, and by LeShack (personal communication) using February 1960 USS* Sargo *data.*

centage (which falls off smoothly) there is an indication of a discontinuous fall-off at about 500 km in Wadhams's observed thick ice percentages. Also, and perhaps more relevant, basin-wide ice roughness contours compiled by LeShack* indicate such an offshore roughness peak in this region.

The relative roles of ridging and growth in maintaining the thick ice near the coast are demonstrated in Figure 19. This figure shows the net ice transfer by ridging and vertical growth at grid cell 2 over an annual cycle together with the thickness distribution on day 129.

---

*Personal communication with L.A. LeShack, LeShack Associates, Silver Spring, Maryland, 1979.

27
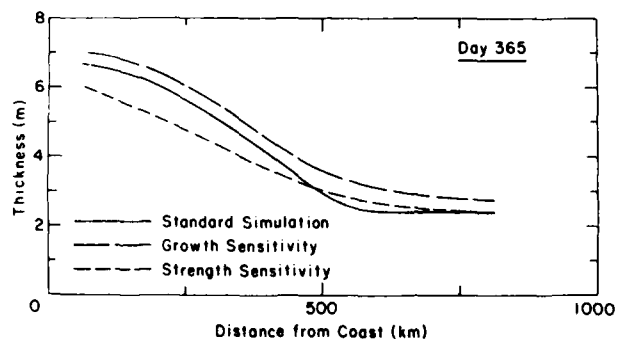
Figure 18. Ice thickness transects through grid cells 2 and 8 for the standard and the two sensitivity simulations.
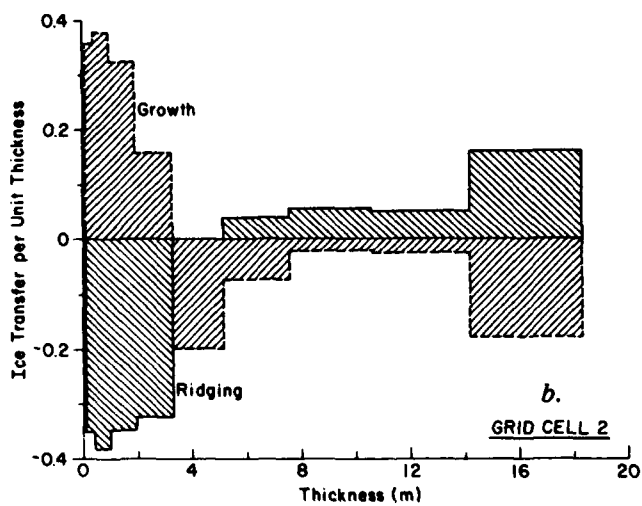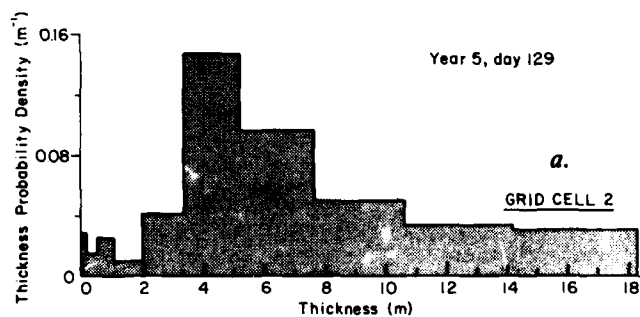
Figure 19. Ice thickness distribution (a) at grid cell 2, and net annual ice transfer probability density (b) owing to growth and ridging at grid cell 2.

28

Over the year, ridging transfers thin ice up to about 3 m thick to thicker categories. The growth, on the other hand, causes a net loss of thick ice. In seasonal equilibrium, imbalances between these two terms are accounted for by advection and deformation (and to a much lesser degree lateral melt). For comparison it is worth noting that plots similar to these yield ice up to only about 2 m being ridged near the North Pole and ice up to only about 1 m being ridged in the southern Beaufort Sea.

Comparison of observed and simulated ice drift

For a direct comparison to observation, the simulated drift rates of three drifting ice stations were determined by interpolation. Table 1 compares some of the simulated deformation rates and net drift to the observed values. The net drift is the average drift from day 140 (1962) to day 109 (1963) of the three drifting ice stations. The x and y strain rates are based on 11-day averaged velocity fields at the ice station locations. Except for the high-strength case, which yields small deformation fluctuations, these comparisons show relatively similar statistical behavior for the simulated deformation rates but significant differences in the long-term drift. Specifically, the simulated net drift for the high strength case is almost half that of the standard case. It is also notable that in the standard simulation the fifth-year net drift is about 30% larger than the first-year because of a gradual reduction in ice strength

Much of the reduction in net drift in the high-strength case is caused by an effective stoppage of almost all motion in April and May. This feature is apparent from Figure 20, which

Figure 20. Simulated and observed drift rates of ice station Arlis (May 1962–April 1963).

29

Table 1. Observed and simulated ice station drift.

	5th year standard simulation	1st year standard simulation	High-strength simulation	High-growth simulation	Observed
Net ice station drift	702 km	567 km	339 km	682 km	562 km
Net drift angle	26 °W	27 °W	13 °W	26 °W	6 °W
Standard deviations of strain rate:					
ϵ_{xx}	0.0033 day^{-1}	0.0038 day^{-1}	0.0028 day^{-1}	0.0035 day^{-1}	0.0028 day^{-1}
ϵ_{yy}	0.0024 day^{-1}	0.0024 day^{-1}	0.0021 day^{-1}	0.0025 day^{-1}	0.0033 day^{-1}
Correlation coefficients between simulated and observed strain rates					
ϵ_{xx}	0.33	0.38	0.31	0.36	—
ϵ_{yy}	0.65	0.65	0.56	0.70	—

Figure 21. Outflow time series for the standard and high-strength simulations. (Units are metres of ice averaged over the basin. For comparison 1.0 m/yr is equivalent to 0.225 Sv.)
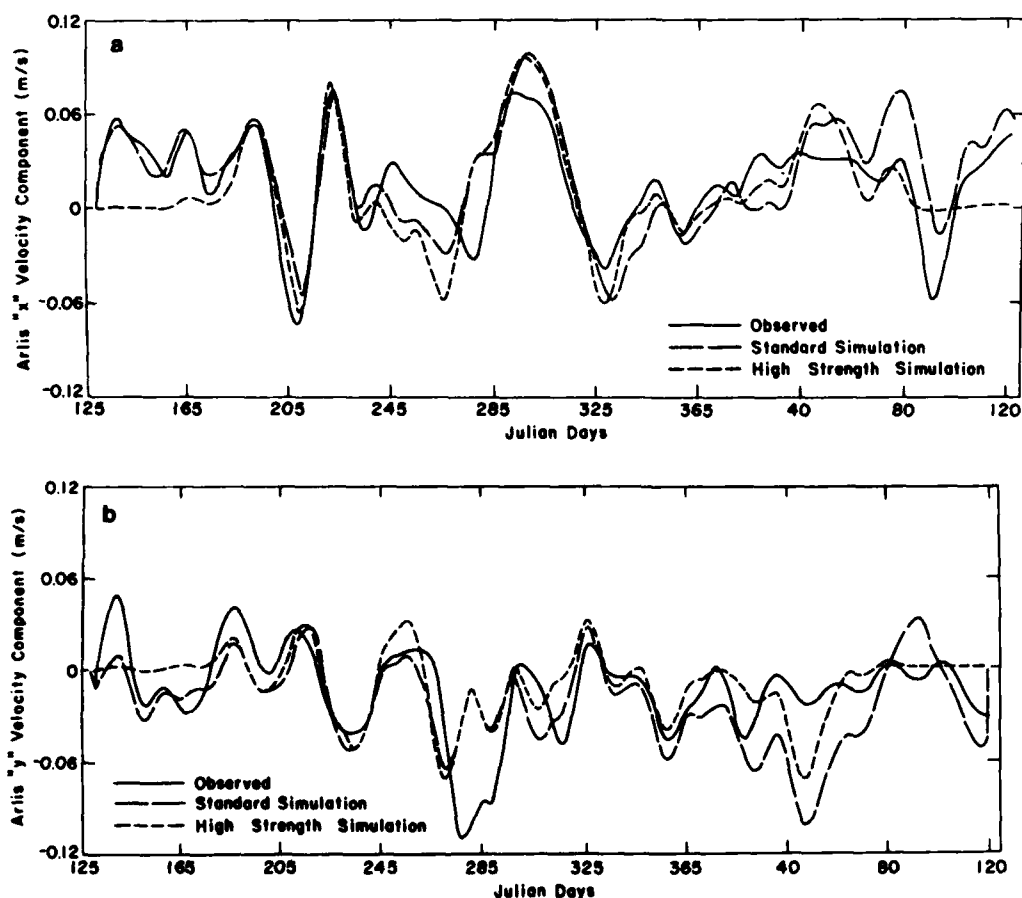
compares the simulated and observed drift rates for ice station Arlis. The ice velocity also stops in the outflow region between Greenland and Spitsbergen, as demonstrated by the ice thickness outflow time series in Figure 21. This "freezing up" of the basin takes place primarily in response to an increase in the ice strength resulting from removal of thin ice by growth and deformation. A secondary effect may be changes in the mean wind patterns as the high pressure system over the Beaufort Gyre weakens and the ice circulation is more dominated by a low pressure system approximately centered over Severnaya Zemlya (Soviet islands at upper-right-hand portion of grid). This low pressure pattern is most pronounced in March when the stoppage begins. There is also some reduction in mean wind speeds in April and May, but this effect appears secondary, as illustrated, for example, by the substantial simulated drift rates of the observed and the standard cases in April and May (Fig. 20).

Temporal variations in ice strength for both the standard and high-strength simulations are shown in Figure 22. The seasonal variation in strength occurs in response to the thermodynamic forcing which in summer melts ice and in winter removes thin ice by freezing. This seasonal variation is consistent with seasonally varying best-fit ice strengths obtained by Hibler and Tucker (1977) and with analysis of ice drift in summer by McPhee (1980b). Note that the main reduction in strength takes place about at day 160 when ice begins melting in the central basin (see Fig. 6). However, in the standard case some seasonal weakening begins earlier. This probably happens because open water created by deformation is not removed by freezing after about day 120. Superimposed on this seasonal variation are fluctuations that

30
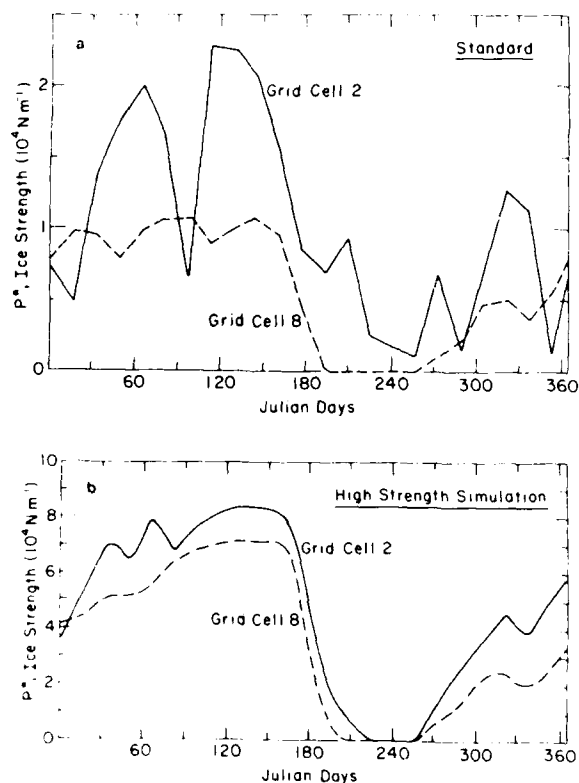
*Figure 22. Ice strength time series for the standard
and high-strength simulations.*

are especially pronounced in the near-shore region. These large fluctuations arise because the
ice strength is determined only by the thinnest 15% of the ice cover (see Appendix A).

It is notable that the standard case strengths are about an order of magnitude higher than
those obtained by Thorndike et al. (1975). While part of this can be attributed to including
frictional losses, the main increase is caused by the way the redistributor used here transfers
thin ice into thicker categories under deformation. It is also notable that the strength range
spanned by the standard and high-strength simulations is similar to the range deduced from
near-shore ice dynamics studies by Pritchard (1978). In particular, using a spatially constant
strength in a localized near-shore region, Pritchard found a best-fit compressive strength of
$\approx 4 \times 10^4$ N m^{-1}. When the compressive strengths were an order of magnitude higher than
this, the ice velocity field was almost entirely determined by the boundary motion. The simu-
lations conducted here indicate that such a dominance by boundary motion can also occur in
a fully coupled, basin-wide dynamic–thermodynamic model when frictional losses in ridging
are sufficiently increased. This result may have relevance to paleoclimate arguments con-
cerning stoppage of the ice flow from the Arctic. In particular, these results suggest that
higher growth rates coupled with a modest increase in frictional losses might cause the basin
to effectively freeze up in winter.

Mass balance characteristics

A dominant feature of the variable thickness model is an increased seasonal variation in
the ice growth and decay. This feature is illustrated in Figure 23, which shows the basin-aver-
aged thickness time series of the standard and thermodynamics-only simulations. While
some of the increased growth is ascribable to a large amount of open water in the fall, much

31

For computation, eq B1 may be rewritten in the form:

$$A_1 + A_2(T_0) + (K/H)(T_w - T_0) = 0 \tag{B2}$$

where A_1 is a constant and $A_2(T_0)$ is a nonlinear function of T_0. Using a Newton-Raphson procedure, one solves eq B2 for T_0. If T_0 is greater than 273.16 K it is set equal to 273.16 K. In both cases the growth rate is then calculated from

$$f_B(H) = -[A_1 + A_2(T_0) + F_0] / Q_l \tag{B3}$$

where Q_l is the volumetric heat of fusion of ice, set at 3.02×10^8 J m^{-3}, and F_0 is a constant oceanic heat flux into the mixed layer from the deep ocean. In the case of open water, eq B3 is also used to estimate the growth rate, with the modification that the albedo is set equal to 0.1, T_0 is set equal to T_w, and the latent heat transfer coefficient D_2 is slightly different. In any given grid cell the water temperature is calculated from the mixed layer equations discussed earlier (eq 6 and 7), and in the presence of the ice is always equal to 271.2 K. Note that while snow cover is not considered explicitly in this model it is easy to determine the growth rate of ice with, say, a snow cover of depth h_s on top. For this purpose (following Semtner [1976]), K in eq B1 and B2 is simply replaced by

$$\frac{K_i}{(h_s/H) + (K_s/K)}$$

where K_s is the snow conductivity.

To examine the behavior of this heat budget code in more detail, the individual components were compiled every 16 days at selected locations. Table B1 lists the components of the heat balance at grid cell 8 for winter growth conditions (18 February), summer melt conditions (26 June), and for a growth–melt transition period (10 June). The atmospheric input values for these times and locations are shown in Table B2. For comparison, also shown in these tables are central Arctic heat balance estimates obtained by Maykut (1978) together with his forcing components.

In making this comparison it should be noted that in addition to different forcing fields there are differences between Maykut's (1978) sea ice thermodynamic formulation and that used here. In particular, for thin ice up to a metre thick, Maykut allows the conductivity to be temperature-dependent and the surface albedo to decrease with thickness. He does, however, assume a steady state equilibrium heat budget. For thick ice (3 m), Maykut uses the

Table B2. Central Arctic (grid cell 8) atmospheric temperatures, dew points and wind speeds.*

	18 February	10 June	16 June
Air temperature (K)	241	269	272
	(242)	(269)	
Wind speed (m s^{-1})	6.17	6.18	1.47
	(5)	(5)	
Dew point temperature (K)	236	268	271

*Central Arctic values used by Maykut are given in parentheses and represent conditions on the first day of the the month. Maykut assumed a relative humidity of 0.90 in February and 0.96 in June.

Table B1. Calculated heat budget components near the Pole for different ice thicknesses in units of centimeters of ice per day* (1 cm of ice per day is equivalent to 34.9537 W m⁻²).

	18 February				10 June				26 June			
		Ice thickness (m)				Ice thickness (m)				Ice thickness (m)		
	Open water	0.5 (0.4)	1.0 (0.8)	4.0 (3.0)	Open water	0.5 (0.4)	1.0 (0.8)	4.0 (3.0)	Open water	0.5 (0.4)	1.0 (0.8)	4.0 (3.0)
Net shortwave radiation	0 (0)	0 (0)	0 (0)	0 (0)	7.5 (8.0)	2.1 (4.4)	2.1 (4.0)	2.1 (1.7)	7.5	3.2	3.2	3.2
Net longwave radiation	− 3.0 (− 4.2)	−0.4 (−1.3)	−0.1 (−1.1)	0.1 (−0.8)	−0.9 (−1.2)	−0.7 (−1.3)	−0.8 (−1.3)	−0.8 (−1.0)	−0.6	−0.9	−0.9	−0.9
Sensible heat flux	−12.3 (−16.5)	−2.5 (−2.2)	−1.5 (−0.9)	−0.5 (0.4)	−0.9 (−0.9)	−0.8 (−1.7)	−0.7 (−1.6)	−0.7 (−0.2)	0	−0.1	−0.1	−0.1
Latent heat flux	− 3.1 (− 4.2)	−0.2 (−0.2)	−0.1 (0)	0 (0)	−0.6 (−0.9)	−0.6 (−1.3)	−0.5 (−1.1)	−0.5 (−0.3)	0	−0.2	−0.2	−0.2
Conductive flux		3.1 (3.7)	1.7 (2.0)	0.4 (0.4)	−0.6 (−0.9)	0 (−0.1)	−0.1 (0)	−0.1 (−0.2)		−0.3	−0.1	0
Growth rate†	18.4 (24.9)	3.1 (3.7)	1.7 (2.0)	0.4 (0.4)	−5.1 (−5.0)	0 (−0.1)	−0.1 (0)	−0.1 (−0.2)	−6.9	−2.0	−2.0	−2.0

* Central Arctic values from Maykut (1978) are given in parentheses.
† Neglecting the oceanic heat flux.

44

APPENDIX B: HEAT BUDGET CODE

To solve for the ice growth rate a surface heat budget computation similar to that of Manabe et al. (1979) and Parkinson and Washington (1979) is used. This heat budget code incorporates a time-independent thermodynamic sea ice model similar to the simplest of a hierarchy of models developed by Semtner (1976). Semtner's simplest time-independent model utilizes a constant conductivity, together with a linear temperature profile. In addition, a seasonal snow cover is allowed to build up and decay. Both the conductivity and the snow-free surface albedo were adjusted by Semtner (1976) to compensate for not including internal melting in summer. With these adjustments, Semtner was able to produce mean annual thicknesses that agreed very well with a more complete time-dependent model developed by Maykut and Untersteiner (1971). In the computations done here, Semtner's (1976) time-independent approach is used. However, following Manabe et al. (1979) the effects of snow cover are approximated only implicitly by changing the surface albedo of the ice to snow values for below-freezing surface temperatures.

The basic surface heat balance equation in the presence of an ice cover is (where fluxes into the surface are considered positive)

$$(1 - \alpha)F_s + F_L + D_1 |U_G| (T_a - T_0) + D_2 |U_G| [q_a(T_a) - q_s(T_0)]$$

$$- D_3 T_0^4 + (K/H)(T_w - T_0) = 0 \tag{B1}$$

where α = surface albedo
T_0 = surface temperature of the ice
T_a = air temperature
K = ice conductivity
H = ice thickness (which for computation is set equal to 0.05 m for very thin ice)
T_w = water temperature
U_G = geostrophic wind
q_a = specific humidity of the air
q_s = specific humidity at the ice surface
F_s = incoming shortwave radiation
F_L = incoming longwave radiation.

The constants D_1 and D_2 are bulk sensible and latent heat transfer coefficients and D_3 is the Stefan-Boltzmann constant times the surface emissivity. Numerical values identical to those used by Parkinson and Washington (1979) are used for these constants. (Specifically, $D_1 = 2.28$ J m^{-3} K^{-1}, $D_3 = 5.50 \times 10^{-8}$ W m^{-2} K^{-4}, $D_2 = 5.69 \times 10^3$ J m^{-3} over water and 6.45×10^3 J m^{-3} over ice.) The specific humidities at the ice (and water) surfaces are calculated in the same manner as described by Parkinson and Washington (1979). Specific humidities and air temperatures at a nominal 10-m reference level above the ice–water surface were obtained from climatological data compiled by Crutcher and Meserve (1970). For the ice albedo 0.616 was used when the surface temperature was equal to 273.16 K. This value is slightly smaller than Semtner's adjusted value of 0.66 but larger than Parkinson and Washington's adjusted value of 0.53 for snow-free ice. For ice with a surface temperature below freezing, $\alpha = 0.75$ was used, which is identical to Parkinson and Washington's "snow" albedo. For the conductivity Semtner's adjusted value of 2.1656 W m^{-1} K^{-1} was used.
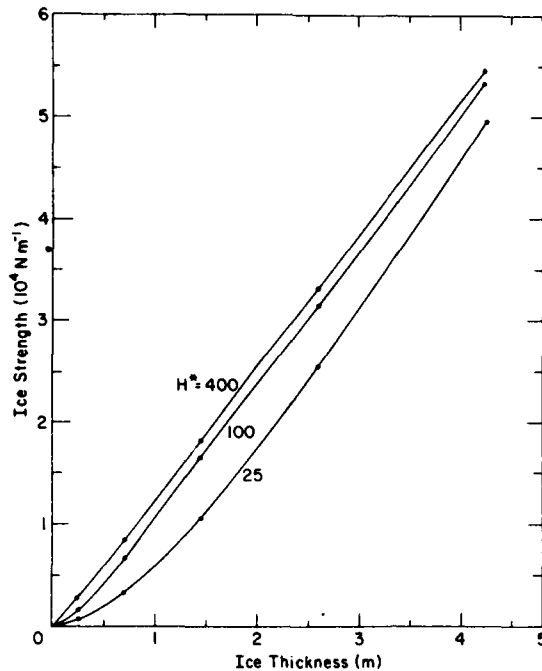
Figure A1. Ice strength versus thickness for the redistributor proposed here. Strengths for different values of the parameter H* (in metres) are shown.

highly dependent on $2H^*$. Consequently, uncertainties in H^* are not critical to the simulations. It is notable that strengths are substantially higher than those obtained by Thorndike et al. In particular, for 25-cm-thick ice, the Thorndike et al. (1975) redistributor would yield a strength of about 5×10^2 N m^{-1} whereas this redistributor yields $\approx 2.5 \times 10^3$ N m^{-1}.

It should be noted that there are some similarities between this redistributor and that proposed by Bugden (1979) and that used in early developments of the ice thickness distribution theory (e.g. Thorndike and Maykut 1973). Bugden's contribution was to show that such a constant redistributor could at least partially be deduced from ridge statistical relations obtained by Hibler et al. (1972) and Mock et al. (1972). The original feature of the redistribution proposed here is that the square root scaling of the maximum thickness cutoff be based on geometric arguments.

where c_1 is a constant, say 0.15. The basic idea here is that under ridging conditions the closure of both thin ice and thick ice occurs; however, the thinnest ice is allowed to be removed to a greater extent. By fixing c_1 to be 0.15, only the thinnest 15% of the ice is deformed. Note that if there is, say, 25% open water, only open water will be removed and there will be no ridging. In the author's judgment this choice of $P(h)$ is quite reasonable and is adopted here with $c_1 = 0.15$.

The other unknown is $\gamma(h_1, h_2)$, which specifies how ice is transferred from one category to another by ridging. Thorndike et al. (1975) have suggested that

$$\gamma(h_1, h_2) = \delta(h_2 - kh_1)(1/k) \tag{A9}$$

where k is a constant. Equation A8 effectively states that ice is transferred into a fixed multiple of its own thickness. This form is computationally simple and is useful for examining the behavior of the ice thickness distribution model. However, the redistribution of eq A8 ignores two important physical features of the ridging. One feature is that under deformation, ridging transfers ice to a variety of thickness categories. This is, for example, evident from field observations of ridges (see, e.g., Weeks et al. 1971, and Kovacs 1972), which show them to be roughly triangular in shape. These observations indicate that under deformation, leads containing thin ice of a given thickness typically form ridges having a triangular cross section. To satisfy eq A9 such ridges would have to have vertical sides.

The second physical feature is that typical ridge heights divided by the thickness of ice being ridged appear to decrease with increasing thickness (see, e.g., Tucker and Govoni 1981). This particular scaling is an important feature of the Parmerter and Coon (1972) mechanistic ridge model. In particular, Parmerter and Coon (1972) found that ridges simulated by using their mechanistic model tended to have a maximum limiting height. This limiting height, however, tended to scale approximately as the square root of the thickness of ice being ridged. Such a square root dependence is also consistent with one's intuition concerning ridging. Consider, for example, two equal width leads undergoing ridging. With the assumption that all the thin ice is deformed into piles of relatively small blocks with similar slope angles, the two ridges formed would have heights scaling with the square root of the thickness of the ice being ridged. If the distribution of lead widths is independent of the ice thickness in leads, such an intuitive argument should have application.

A number of redistributors could be constructed that approximately satisfy these constraints. However, the simplest case is to take γ to be a constant up to some cutoff thickness:

$$\gamma(h_1, h_2) = C_2 \text{ for } 2h_1 \leq h_2 \leq b(h_1)h_1 \tag{A10}$$

where

$$b(h_1) = 2(H^*/h_1)^{1/2}$$

with H^* a constant. Examination of Parmerter and Coon's (1972) mechanistic studies suggests that $H^* = 100$ m is a reasonable value. For 1-m-thick ice this yields a maximum ridged ice thickness of 20 m. What type of strengths this yields is illustrated in Figure A1, which shows typical ice strengths (obtained numerically) versus thickness for this redistributor. For comparison, strengths for several different values of H^* are shown. (Since ice thicker than 18.3 m is not allowed numerically, the thick ice strengths in Figure A1 will be somewhat smaller than analytical values obtained in the *Analytic Examination of the Ridge Redistribution Process* section.) An item of particular interest for this paper is that the strengths are not

41

$$\int\limits_0^\infty \left[P(h)\,g(h) - \int\limits_0^\infty \gamma(h',h)\,P(h')\,g(h')\,dh' \right] dh. \tag{A5}$$

The first term in eq A4 specifies the amount of open water created, while the second term describes the transfer of thin ice to thicker categories by ridging. In this formalism $\gamma(h_1, h_2)dh_2$ can be thought of as the area of ice put into the thickness interval $[h_2, h_2 + dh_2]$ when a unit area of ice of thickness h_1 is used up. Basically, the integral over γ specifies where the ice is transferred to during ridging. The function $P(h)$, on the other hand, is some probability function specifying which categories are being destroyed by ridging. Written in this form γ automatically satisfies eq A1. Satisfaction of eq A2 and A3 leads to the additional constraints, respectively,

$$\int\limits_0^\infty \gamma(h', h)\,h\,dh = h' \tag{A6}$$

$$C \int\limits_0^\infty W_r h^2 dh = P^*. \tag{A7}$$

Equation A6 requires that transfer of ice from the category does not change its mass, and eq A7 serves as a definition of the ice strength P^*.

To get some feeling for the amount of open water created with this formulation, it is useful to explicitly calculate the coefficients in eq A4. The dynamical code used here employs an elliptical yield curve (see Hibler 1979). Using this particular rheology (and noting that the symbol P in eq 4 of Hibler [1979] is equivalent to the symbol P^* used here) one can easily show that:

$$(\sigma_{ij}\dot{\epsilon}_{ij})/P^* = 0.5(\Delta - \dot{\epsilon}_{kk})$$

where

$$\Delta = [(\dot{\epsilon}_{11}^2 + \dot{\epsilon}_{22}^2)(1 + 1/e^2) + 4e^{-2}\dot{\epsilon}_{12} + 2\dot{\epsilon}_{11}\dot{\epsilon}_{22}(1 - 1/e^2)]^{1/2}.$$

Note that Δ is dependent only on the two invariants of the strain rate tensor: $\dot{\epsilon}_I = (\dot{\epsilon}_{11} + \dot{\epsilon}_{22})$ and $\dot{\epsilon}_{II} = [(\dot{\epsilon}_{22} - \dot{\epsilon}_{11})^2 + 4\dot{\epsilon}_{12}^2]$. In this expression, e is the ratio of the principal axes of the elliptical yield curve (set equal to 2) and is a measure of the relative shear strength to compressive strength. Larger e values yield less shear strength. With this rheology no open water will be formed under pure convergence ($\dot{\epsilon}_{11} = \dot{\epsilon}_{22}; \dot{\epsilon}_{12} = 0; \dot{\epsilon}_{11} < 0$). Conversely, under pure divergence ($\dot{\epsilon}_{11} = \dot{\epsilon}_{22}; \dot{\epsilon}_{12} = 0; \dot{\epsilon}_{11} > 0$) there will be no ridging. Also, as $e \to \infty$ the amount of open water forming under pure shear ($\dot{\epsilon}_{11} = \dot{\epsilon}_{22} = 0; \dot{\epsilon}_{12} \neq 0$) will approach zero. In the Thorndike et al. (1975) study the special case of $e = 1$ was used.

The two main unknowns in the redistribution theory are $P(h)$ and $\gamma(h_1, h_2)$. Thorndike et al. (1975) have suggested that $P(h)$ be given by

$$P(h) = \text{Max}\left[\left(1 - \int\limits_0^h g(h)\,dh/c_1\right), 0 \right] \tag{A8}$$

APPENDIX A: MECHANICAL REDISTRIBUTOR

Consider a two-dimensional continuum with ice that is described by a plastic rheology such that the stress state $\sigma_{ij}(\dot{\epsilon}_{ij}, P^*)$ is a function of the strain rate $\dot{\epsilon}_{ij}$ and a strength P^*. Then, following Thorndike et al. (1975) and Rothrock (1975), the mechanical redistribution function ψ (see eq 4) must satisfy the following constraints:

$$\int_0^\infty \psi\, dh = \nabla \cdot \underline{u} \tag{A1}$$

$$\int_0^\infty h\psi\, dh = 0 \tag{A2}$$

$$C \int_0^\infty h^2 \psi(h)dh = \sum_{ij} \sigma_{ij}\dot{\epsilon}_{ij} \tag{A3}$$

where $\underline{u}$ is the ice velocity field and C is a constant. In consideration of only the work done on the ice by gravitational buoyancy forces, C would be given by

$$C_b = \tfrac{1}{2}\, \varrho_i \left| [(\varrho_w - \varrho_i)/\varrho_w] g \right|$$

with ϱ_i the density of ice, ϱ_w the density of water, and g the acceleration of gravity. Equation A1 follows from the constraint that ψ renormalize the g distribution to unity because of changes in area. Equation A2 follows from conservation of mass and basically states that ψ does not create or destroy ice but merely changes its distribution. (An additional assumption in eq A2 is that the ice mass is related in a fixed manner to the thickness.) The third constraint (Rothrock 1975) specifies that work done in building ridges is equal to the deformational work. An important feature of this constraint is that, for an arbitrary plastic yield curve, it forces some ridging to take place even though there may be no net convergence. In its present form (with $C = C_b$) eq A3 ignores frictional losses occurring in ridging and considers only the potential energy change from deformed ice being lifted against gravity and being forced down against buoyancy. However, Rothrock (1975) has estimated these frictional losses to be the same order of magnitude as the potential energy changes. Consequently, as a crude approximation for frictional losses, eq A3 is retained here with a constant C equal to $2C_b$.

As in Thorndike et al. (1975), a redistribution that satisfies these constraints is (using the convention that repeated subscripts are summed over)

$$\psi = \delta(h)\, [(1/P^*)\sigma_{ij}\dot{\epsilon}_{ij} + \dot{\epsilon}_{kk}] + (1/P^*)\sigma_{ij}\dot{\epsilon}_{ij} W_r(h,g) \tag{A4}$$

where

$$W_r(h,g) = \left[-P(h)\, g(h) + \int_0^\infty \gamma(h',h)\, P(h')\, g(h')dh' \right] /$$

39

Thorndike, A.S., D.A. Rothrock, G.A. Maykut and R. Colony (1975) The thickness distribution of sea ice. *Journal of Geophysical Research,* **80:** 4501-4513.

Tucker, W.B., III and J.W. Govoni (1981) Morphological investigations of first-year sea ice pressure ridge sails. *Cold Regions Science and Technology,* **5:** 1-12.

Tucker, W.B., III, W.F. Weeks and M. Frank (1979) Sea ice ridging over the Alaskan continental shelf. *Journal of Geophysical Research,* **84:** 4885-4897.

Vinje, T.E. (1976) Sea ice conditions in the European sector of the marginal seas of the Arctic, 1966-1975. Oslo: Norsk Polar Institutt Arbok 1975, pp. 163-174.

Wadhams, P. (1981) Sea ice topography of the Arctic Ocean in the region 70°W to 25°E. *Philosophical Transactions of the Royal Society of London, Series A,* **302:** 45-85.

Wadhams, P. (1980) Ice characteristics in the seasonal sea ice zone. *Cold Regions Science and Technology,* **2:** 37-88.

Wadhams, P., A.E. Gill and P.F. Linden (1979) Transects by submarine of the East Greenland polar front. *Deep-Sea Research,* **26A:** 1311-1327.

Walsh, J.E. and C.M. Johnson (1979a) Interannual atmospheric variability and associated fluctuations in arctic sea ice extent. *Journal of Geophysical Research,* **84:** 6915-6928.

Walsh, J.E. and C.M. Johnson (1979b) An analysis of arctic sea ice fluctuations, 1953-77. *Journal of Physical Oceanography,* **9:** 580-591.

Washington, W.M., A.J. Semtner, C. Parkinson and L. Morrison (1976) On the development of a seasonal change sea-ice model. *Journal of Physical Oceanography,* **6:** 679-685.

Weeks, W.F., A. Kovacs and W.D. Hibler III (1971) Pressure ridge characteristics in the arctic coastal environment. *Proceedings of First International Conference on Port and Ocean Engineering Under Arctic Conditions.* Vol. 1. Trondheim, Norway: Technical University of Norway, pp. 152-193.

Wittman, W.I. and J.J. Schule (1966) Comments on the mass budget of arctic pack ice. In *Proceedings of the Symposium on the Arctic Heat Budget and Atmospheric Circulation.* Rand Memo. RM-5233-NSF. Santa Monica, Calif.: Rand Corporation, pp. 215-246.

Zillman, J.W. (1972) A study of some aspects of the radiation and heat budgets of the Southern Hemisphere oceans. *Meteorolgical Studies.* Vol. 26. Canberra, Australia: Bureau of Meteorology, Department of the Interior.

Zubov, N.N. (1945) *Arctic Ice.* Moscow: Izdatel'stvo Glavsevmorputi. (English translation by U.S. Navy Oceanography Office/American Meteorological Society.)

Lemke, P., E.W. Trinkl and K. Hasselmann (1980) Stochastic dynamic analysis of polar sea ice variability. *Journal of Physical Oceanography*, 10· 2100–2120.

LeShack, L.A., W.D. Hibler III and F.H. Morse (1971) Automatic processing of arctic pack ice obtained by means of submarine sonar and other remote sensing techniques. In *Propagation Limitations in Remote Sensing* (J.B. Lomax, Ed.). AGARD Conference Proceedings, No. 90, 5-1 to 5-19. [NTIS AGARD-CP-90-71.]

McPhee, M.G. (1980a) A study of oceanic boundary-layer characteristics including inertial oscillations at three drifting stations in the Arctic Ocean. *Journal of Physical Oceanography*, 10(6): 870–884.

McPhee, M.G. (1980b) An analysis of pack ice drift in summer. In *Sea Ice Processes and Models* (R.S. Pritchard, Ed.). Seattle: University of Washington Press, pp. 62–75.

Manabe, S. and R. Stouffer (1980) Sensitivity of a global climate model to an increase of CO_2-concentration in the atmosphere. *Journal of Geophysical Research*, 85: 5529–5554.

Manabe, S., K. Bryan and M.J. Spelman (1979) A global ocean-atmosphere climate model with seasonal variation for future studies of climate sensitivity. *Dynamics of Atmosphere and Oceans*, 3: 393–426.

Martin, S. (1979) A field study of brine drainage and oil entrainment in first-year sea ice. *Journal of Glaciology*, 22: 473–502.

Maykut, G.A. (1978) Energy exchange over young sea ice in the central arctic. *Journal of Geophysical Research*, 83: 3646–3658.

Maykut, G.A. and N. Untersteiner (1971) Some results from a time-dependent, thermodynamic model of sea ice. *Journal of Geophysical Research*, 76: 1550–1575.

Mesinger, F. and A. Arakawa (1976) Numerical methods used in atmospheric models. Global Atmospheric Research Program Publication Series, No. 17, Geneva.

Mock, S.J., A.D. Hartwell and W.D. Hibler III (1972) Spatial aspects of sea ice ridge distributions. *Journal of Geophysical Research*, 77: 5945–5953.

Parkinson, C.L. and W.M. Washington 1979) A large-scale numerical model of sea ice. *Journal of Geophysical Research*, 84: 311–337.

Parmerter, R.R. and M.D. Coon (1972) Model of pressure ridge formation in sea ice. *Journal of Geophysical Research*, 77: 6565–6575.

Pritchard, R.S. (1978) The effect of strength on simulations of sea ice dynamics. *Proceedings of Fourth International Conference on Port and Ocean Engineering Under Arctic Conditions* (D.E. Muggeridge, Ed.). Newfoundland: Memorial University of St. Johns, pp. 494–505.

Pritchard, R.S., M.D. Coon and M.G. McPhee (1977) Simulation of sea ice dynamics during AIDJEX. *Journal of Pressure Vessel Technology*, 99J: 491–497.

Rogers, J.C. (1978) Meteorological factors affecting interannual variability of summertime ice extent in the Beaufort Sea. *Monthly Weather Review*, 126: 890–897.

Rothrock, D.A. (1979) Modeling sea ice features and processes. *Journal of Glaciology*, 24: 359–376.

Rothrock, D.A. (1975) The energetics of the plastic deformation of pack ice by ridging. *Journal of Geophysical Research*, 80: 4514–4519.

Saltzman, B. and R.E. Moritz (1980) A time-dependent climatic feedback system involving sea-ice extent, ocean temperature, and CO_2. *Tellus*, 32: 93–118.

Semtner, A.J., Jr. (1976) A model for the thermodynamic growth of sea ice in numerical investigations of climate. *Journal of Physical Oceanography*, 6: 379–389.

Thorndike, A.S. and G.A. Maykut (1973) On the thickness distribution of sea ice. *AIDJEX Bulletin*, 21: 31–48.

Thorndike, A.S. and R. Colony (1980) Large-scale ice motion in the Beaufort Sea during AIDJEX, April 1975–April 1976. In *Sea Ice Processes and Models* (R.S. Pritchard, Ed.). Seattle: University of Washington Press, pp. 249–260.

Bugden, G.L. (1979) The deformation of pack ice by ridging. *Journal of Geophysical Research*, **84**: 1793-1796.

Coachman, L.K. and K. Aagaard (1974) Physical oceanography of arctic and subarctic seas. In *Marine Geology and Oceanography of the Arctic Seas* (Y. Herman, Ed.). New York: Springer-Verlag, pp. 1-72.

Coon, M.D. (1974) Mechanical behavior of compacted arctic ice floes. *Journal of Petroleum Technology*, **26**: 446-470.

Coon, M.D., R. Colony, R. S. Pritchard and D.A. Rothrock (1976) Calculations to test a pack ice model. *Numerical Methods in Geomechanics*. Vol. 2 (G.S. Desai, Ed.). New York: American Society of Civil Engineers, pp. 1210-1227.

Crutcher, H.L. and J.M. Meserve (1970) Selected level heights, temperatures and dew points for the Northern Hemisphere. NAVAIR50-1C-52, Revised. Washington, D.C.: Naval Weather Service Command.

Gordienko, P. (1958) Arctic ice drift. In *Proceedings of Conference on Arctic Sea Ice*. Washington, D.C.: National Academy of Sciences and National Research Council, Publication 598, pp. 210-220.

Herman, G.F. and W.T. Johnson (1978) The sensitivity of the general circulation to arctic sea ice boundaries: A numerical experiment. *Monthly Weather Review*, **106**: 1649-1664.

Hibler, W.D., III (1979) A dynamic/thermodynamic sea ice model. *Journal of Physical Oceanography*, **9**: 815-846.

Hibler, W.D., III (1980a) Documentation for a two-level dynamic thermodynamic sea ice model. U.S. Army Cold Regions Research and Engineering Laboratory, CRREL Special Report 80-8.

Hibler, W.D., III (1980b) Sea ice growth, drift and decay. In *Dynamics of Snow and Ice Masses* (S. Colbeck, Ed.). New York: Academic Press, pp. 141-209.

Hibler, W.D., III (1980c) Modeling a variable thickness sea ice cover. *Monthly Weather Review*, **108**(12): 1943-1973.

Hibler, W.D., III, W.F. Weeks and S.J. Mock (1972) Statistical aspects of sea-ice ridge distributions. *Journal of Geophysical Research*, **77**: 5954-5970.

Hibler, W.D., III, S.J. Mock and W.B. Tucker III (1974) Classification and variation of sea ice ridging in the western Arctic Basin. *Journal of Geophysical Research*, **79**: 2735-2743.

Hibler, W.D., III and W.B. Tucker III (1977) Seasonal variations in apparent sea ice viscosity on the geophysical scale. *Geophysical Research Letters*, **4**: 87-90.

Huschke, R.E. (1969) Arctic cloud statistics from "air-calibrated" surface weather observations. Memo. RM-6173-PR (unpublished). Santa Monica, Calif.: Rand Corporation.

Idso, S.B. and R.D. Jackson (1969) Thermal radiation from the atmosphere. *Journal of Geophysical Research*, **74**: 5397-5403.

Koerner, R.M. (1973) The mass balance of the sea ice of the Arctic Ocean. *Journal of Glaciology*, **12**: 173-185.

Kovacs, A. (1972) On pressured sea ice. In *Sea Ice: Proceedings of an International Conference*. Reykjavik, Iceland: National Research Council of Iceland, pp. 276-295.

Kovacs, A. and M. Mellor (1974) Sea ice morphology and ice as a geologic agent in the southern Beaufort Sea. In *The Coast and Shelf of the Beaufort Sea* (J.L. Reed and J.E. Sater, Ed.). Washington, D.C.: Arctic Institute of North America, pp. 113-161.

Kurihara, Y. (1965) On the use of implicit and iterative methods for the time integration of the wave equation. *Monthly Weather Review*, **93**: 33-46.

Langleben, M.P. (1971) Albedo of melting sea ice in the southern Beaufort Sea. *Journal of Glaciology*, **10**: 101-104.

Langleben, M.P. (1972) The decay of an annual cover of sea ice. *Journal of Glaciology*, **11**: 337-344.

The interannual evolution of the summer ice edge is, on the other hand, dominated by thermodynamic growth and decay rates rather than ridge buildup. Specifically, lower annual thermodynamic net growth coupled with offshore ice advection gradually thins the ice off the North Slope and Siberian coasts. This thin ice presence, coupled with high summer melting rates, creates an excessive ice edge in summer. Sensitivity analyses show that the magnitude of this summer ice edge is critically dependent on the albedo used for melting sea ice. By modifying this albedo by only about 10%, much more realistic ice edge values may be obtained. Similarly, small changes in the open water albedo should lead to substantially improved summer ice margins. These ice edge results emphasize the need for a more detailed analysis of the thermodynamic sensitivity of such variable thickness sea ice models. One approach is to do some process sensitivity studies using observed ice motion estimates as driving fields. Another approach would be to compare observed and simulated ice edge results over several sequential years.

The heat exchange characteristics simulated here are substantially affected by sea ice ridging and deformation. On a basin-averaged scale, ridging transfers thin ice to thicker categories, thus making room for more thin ice to form. The thicker ice thus formed grows slowly in winter, but ablates rapidly in summer. Spatial imbalances between ridging and open water creation cause substantial spatial variations in the air–sea heat exchange. Regions with more ridging tend to have a net heat gain from the atmosphere. Regions of large open water creation, on the other hand, have more growth and thus have a net loss of heat to the atmosphere. These variations are in contrast to thermodynamic simulations, where in equilibrium the net annual ice growth is zero everywhere.

In coupled dynamic–thermodynamic sea ice models, the way in which thin ice is statistically redistributed into thicker ice can significantly affect the geophysical stresses in pack ice. The agreement with ridge morphological data and the realistic simulated ice thickness and ridge buildup support the redistribution function proposed here. However, a major unknown factor is the amount of frictional energy lost during ridging. The strengths simulated here were realistic, although a bit small. But, sensitivity analysis suggests that only a modest increase in frictional losses during ridging would be adequate for more realistic ice velocities and strengths. Since frictional losses in ridging are not precisely known, such increases are physically justifiable. Sensitivity studies with more detailed ice velocity verification fields should help determine necessary strength increases more precisely. Polar drifting buoy data taken should prove helpful in such studies.

LITERATURE CITED

Aagaard, K. and P. Greisman (1975) Toward new mass and heat budgets for the Arctic Ocean. *Journal of Geophysical Research,* **80**:3821-3827.

Ackley, S.F., A.J. Gow, K.R. Buck and K.M. Golden (1980) Sea ice studies in the Weddell Sea aboard USCGC *Polar Sea. Antarctic Journal of the United States,* **15**(5): 84-86.

Andreas, E.L. (1980) Estimation of heat and mass fluxes over arctic leads. *Monthly Weather Review,* **108**(12): 2057-2063.

Barnett, D.G. (1980) A long-range ice forecasting method for the north coast of Alaska. In *Sea Ice Processes and Models* (R.S. Pritchard, Ed.). Seattle: University of Washington Press, pp. 360-372.

Bryan, K. (1969) A numerical method for the study of the circulation of the world oceans. *Journal of Computational Physics,* **4**: 347-376.

Bryan, K., S. Manabe and R.L. Pacanowski (1975) A global ocean-atmosphere climate model. Part II, The ocean circulation. *Journal of Physical Oceanography,* **5**: 30-46.
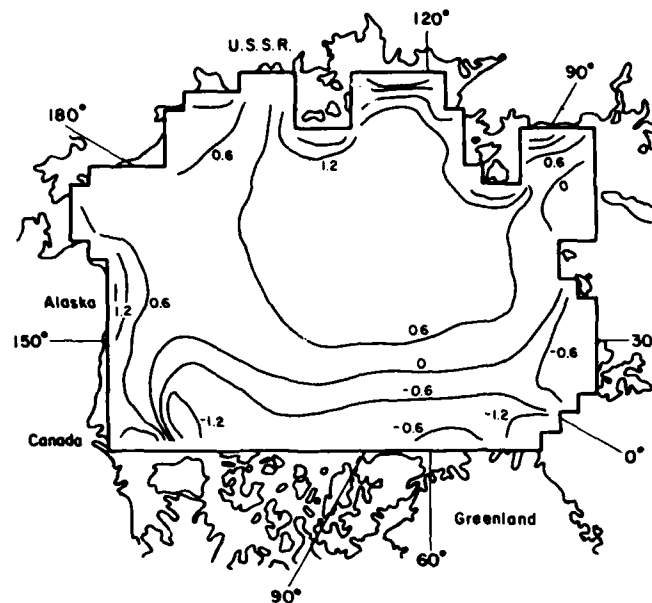
Figure 25. Annual net growth contours (at 0.6-m intervals) for the standard simulation.

thin ice to occur by divergence along one coast while converging ice into thicker categories at another coast. The thicker ice ablates faster in summer than it freezes in winter, while the reverse is true of thin ice. As a consequence, over an annual cycle (neglecting oceanic effects) areas with high ridging will have a net heat gain from the atmosphere and divergent thin ice regions will have a net loss.

CONCLUDING REMARKS

This report describes a variable thickness dynamic–thermodynamic sea ice model and examines the seasonal equilibrium characteristics of this model. To develop this model, the Thorndike et al. (1975) ice thickness distribution framework was extended to include an oceanic mixed layer at a fixed depth and lateral melting effects. In addition, a mechanical redistribution process that is consistent with hypothesized and observed physics of the ridging process has been proposed. By combining this framework with a viscous-plastic ice dynamics model that was developed previously (Hibler 1979) and a spatially varying surface heat budget, seasonal equilibrium simulations may be performed.

A dominant feature of the Arctic simulations discussed here is the time needed for the thickness characteristics to fully evolve. The main characteristic is a buildup of ice along the Canadian Archipelago in conjunction with a thinning of ice off the Alaskan and Siberian coasts. These geographical chan ..., however, take several years to fully develop. Off the Archipelago, the buildup is based upon an accumulation of ridged ice formed over several years. During each year the ice strength builds up as thin ice is removed by ridging and growth. This creates a balance between the internal and external stresses. Since the thick ice does not directly affect the ice stresses, its equilibrium balance requires a longer time scale. Once equilibrium is reached, summer ablation of the thick ice largely offsets the new thick ice formed by ridging.
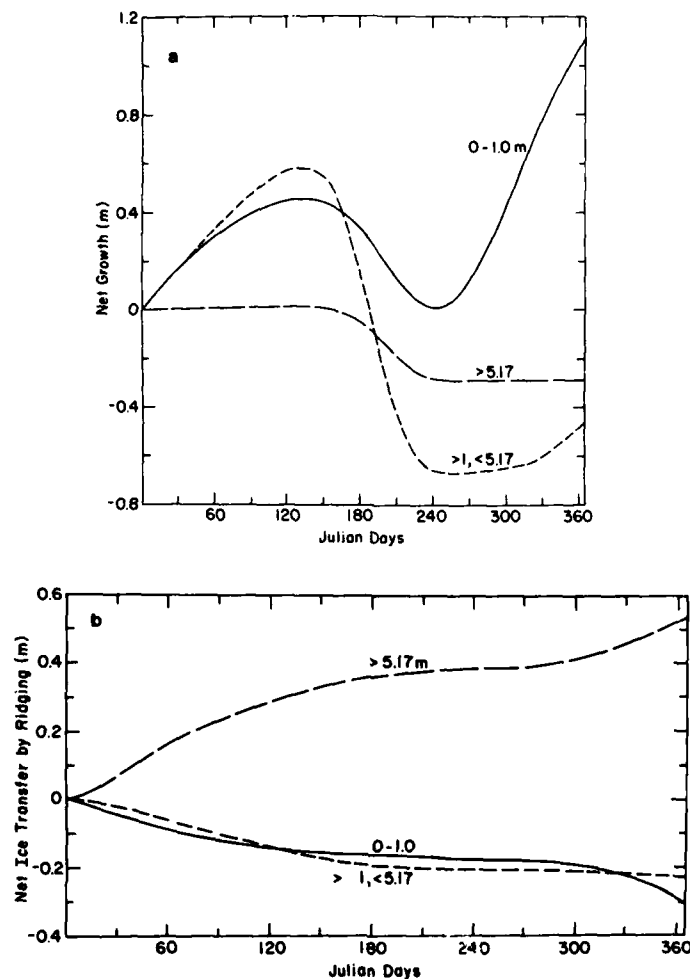
34

*Figure 24. Basin-averaged net ice growth (a) and net ice trans-
fer by ridging (b) for three categories of ice in the standard
simulation.*

also be that not enough open water is being created owing to inadequate temporal and spatial
resolution of the wind fields. For example, while the basin-averaged thin ice growth (1 m) ap-
proximately equals thicker ice growth in January, the ice growth in the central basin in con-
siderably less. From day 1 to day 60, thin ice growth at grid cells 7 and 8 accounted for only
about 20% of the ice growth. These values are substantially less than estimates by Maykut
(1978), which yield approximately equivalent growth by thin and thick ice in the central basin
in winter.

In addition to increasing the total air–sea heat exchange by ridging and open water crea-
tion, the dynamics also causes a spatial imbalance in the heat exchange. Because of this im-
balance, the net growth over an annual cycle will not be zero everywhere, as in a thermo-
dynamics-only simulation, but will vary spatially. These variations can be very significant as
demonstrated in Figure 25. This imbalance can occur by freezing ice at one location and then
transferring it to another where it is melted. However, in practice the process is more com-
plex and it relies upon ridging to a large extent. The ice dynamics, for example, can cause
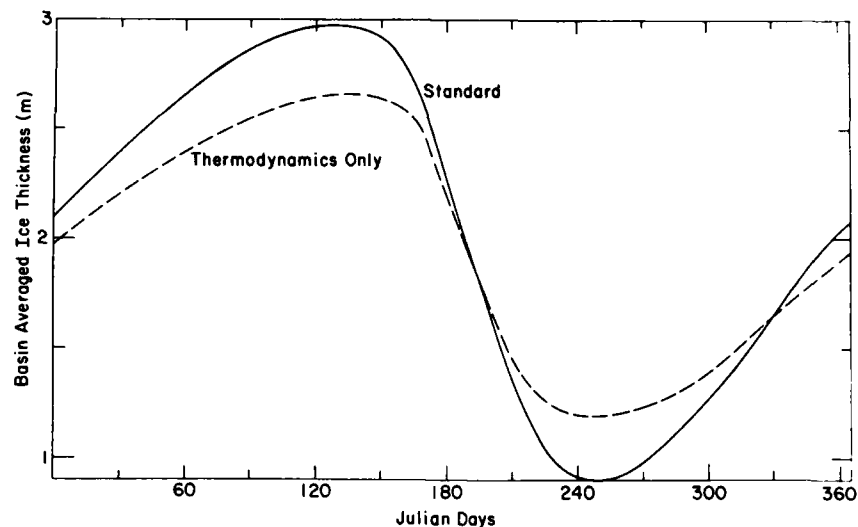
33

Figure 23. Basin-averaged ice thickness time series for the standard and thermodynamics-only simulations.

is from thin ice created by deformation. The increased decay rates, on the other hand, arise because of higher heat absorption by open water and by loss of ice from the basin by outflow. Some of these characteristics are illustrated in Figure 24, where the basin-averaged net growth and net ice transfer by ridging are plotted for three broad ice categories. On a basin-averaged basis, open water creation is balanced by ridging, which transfers thin ice to the thick ice categories. Consequently, the large amount of fall and winter ridging shown in Figure 24 indicates that a large amount of open water is also being created then. With regard to decay, on day 180 the standard case has 25% open water, as contrasted to no open water for the thermodynamic case. Also, the net annual export of ice from the basin amounts to about 0.09 Sv, a value close to that estimated by Aagaard and Greisman (1975). For comparison, the net outflow in the high-strength case amounts to only about 0.045 Sv. Note, however, that the outflow rates do fluctuate substantially (Fig. 21), a feature that is commensurate with observations by Vijne (1976).

In general, Figure 24 illustrates the important role ridging plays in the mass balance. On the average, ridging transfers thin and intermediate ice to thicker categories, thus making room for thinner ice and, hence, greater growth. This transfer, in turn, offsets the ablation of the thicker ice. Note that there is an annual net ablation of thick and intermediate ice. By analyzing the transfer by growth as well as by ridging, it can be shown that the net intermediate ice melt is partially offset by increased vertical growth as well as by outflow and ridging. However, the thick ice net melt is almost all balanced by ridging and outflow.

While there are certain quantitative differences, these mass balance results are qualitatively similar to observational estimates by Koerner (1973). Based mostly on ground observations in the central basin, Koerner (1973) deduced a total annual ice growth of about 1.1 m, peaking in a thickness of about 3.7 m. He estimated this growth to be balanced by about 0.7 m of outflow and 0.4 m of ablation. Koerner also determined that about 40% of the ice grew over ice less than 1 m thick, and that 0.20 m of the new ice ended up in ridges. The simulations performed here yield a similar dominance of growth by thin ice (and concomitant incorporation of new ice in ridges) but yield a smaller maximum ice thickness. Also, there is substantially more ablation and melting. Part of this difference is likely from a more complete inclusion of peripheral areas of the basin in the simulated estimates. However, it may

32

time-dependent Maykut–Untersteiner (1971) model and includes a seasonal snow cover. In addition, larger values for the sensible and latent heat bulk aerodynamic coefficients are used. (The smaller values used by Parkinson and Washington [1979], and hence here, can be justified because geostrophic rather than surface wind speeds are being input.)

In the February case the dominant characteristic in the heat balance is a rapid decrease in the sensible and latent heat components as the ice thickens. The ice sensible heat losses simulated here are somewhat larger than Maykut's values, primarily due to a larger amount of incoming longwave radiation. (The difference in incoming longwave radiation may be deduced by examining the open water case.) The larger radiation used here tends to give a higher surface ice temperature and, hence, a greater sensible heat loss. This is especially pronounced in the case of thick ice, where Maykut's smaller longwave radiation allows the surface temperature of the snow-covered ice to drop below the air temperature, and, hence, change the sign of the sensible heat transfer.

In the growth-melt transition case, the main difference is in the net shortwave radiation terms. The smaller thin ice albedos used by Maykut give a greater absorption of shortwave radiation. This in turn results in a greater surface temperature and larger sensible heat flux than in the simulation performed here. This condition is, however, reversed in the very thick ice, where a Maykut snow albedo greater than 0.75 allows less shortwave radiation to be absorbed. Note also that in this transition period the sensible heat loss is less dependent upon thickness. This arises from the smallness of the conductivity term (which characterizes the ice thickness), ascribable to a small temperature differential.

It is notable that despite differences in parameterization and forcings, the simulated ice growth rates are relatively similar in both the February and June cases. This demonstrates the negative feedback character of the heat budget in the presence of an ice cover. Basically, the system attempts to minimize the effect of changes of one component by the adjustment of other components. Larger incoming longwave radiation will, for example, be offset partially by a greater surface temperature (which in turn causes more outgoing radiation) and p⁻ ially by an increased sensible heat loss. In the open water case these feedbacks cannot operate since the surface temperature is fixed.

Finally, in the 26 June case the surface temperature in all the ice cases is fixed at freezing. As a consequence the ice melting rate is independent of thickness, since all snow-free ice albedos are assumed equal. There is a difference in conduction, with the thinner ice having slightly greater conduction of heat into the mixed layer and, hence, more bottom melting. Note, however, that in all cases most of the melting is surface ablation. The greater heat absorption of the open water arises from its lower albedo.

APPENDIX C: THICKNESS FINITE DIFFERENCE CODE

Thickness partition

For the thickness differencing, an arbitrary number of irregularly spaced thickness levels are employed with a center thickness h_i and thickness limits h_i' to h_{i+1}'. Open water is considered simply by having one thickness category centered at zero thickness. In order to avoid discontinuities, the thickness mesh is forced to vary smoothly. A flexible procedure used in certain numerical ocean models (vis Bryan 1969) is to allow the spacing between categories to vary according to a Gaussian distribution.* Using this procedure, one obtains a partition of center thicknesses by

$$h_m = \begin{cases} 0 & \text{for } m = 1 \\ h_{m-1} + c_1 + c_2\{1 - \exp[-(m-1)^2/c_3]\} & \text{for } m \neq 1 \end{cases} \tag{C1}$$

where c_1, c_2 and c_3 are constants. Thickness limits are then determined by

$$h_m' = \begin{cases} (h_1 - c_1)/2 & \text{for } m = 1 \\ 2h_{m-1} - h_{m-1}' & \text{for } m > 1. \end{cases} \tag{C2}$$

Clearly, by varying c_1, c_2 and c_3 a wide variety of different thickness partitions may be obtained. The particular arrangement used in these simulations (see Fig. 1) was by using $c_1 = 0.2$ m, $c_2 = 7.0$ m, and $c_3 = 110$.

By use of this thickness partition, the areal thickness distribution is defined at the interior of the thickness interval h_i' to h_{i+1}' and is denoted by g_i. For computation, an auxiliary dimensionless distribution function $\tilde{g}_i$ is defined by

$$\tilde{g}_i = \Delta h_i \, g_i$$

where $\Delta h_i = h_{i+1}' - h_i'$. For future differencing, $\tilde{g}_i$ is considered to have a mean thickness of h_i. The definition of $\tilde{g}_i$ is that it is the fraction of area covered by ice with thickness between h_i' and h_{i+1}'. The growth rates for each category are also defined at the interior of the thickness category and are denoted by $f_i = f(h_i)$.

Thickness finite differencing

To carry out the operations in the time marching equations (eq 10–15) it is necessary to have thickness finite differences for the term $(f\tilde{g})_h$, where the subscript h denotes a thickness finite difference. In addition, a finite difference procedure is needed for the redistribution and the lateral melting. The finite differences for the lateral melting steps are relatively trivial. In particular, integrals over g are simply replaced by sums over $\tilde{g}_i$. However, the other terms are more complex. Consequently, the differencing schemes for the $(fg)_h$ term and the redistribution are described here. The other spatial finite differences are identical to those used by Hibler (1979) and are described there.

* Personal communication with M. Cox, Geophysical Fluid Dynamics Laboratory, Princeton, New Jersey, November 1979.

There are two constraints that must be preserved by the finite difference $(\tilde{f}g)_h$. One is that the sum of the changes in $\tilde{g}$ are zero. This follows from the fact that vertical growth does not change the total area of ice and open water. The second is that the new total thickness must differ from the old thickness by an amount equal to the ice grown (or melted). These constraints can be expressed in finite difference form by (where M thickness levels are assumed)

$$\sum_{i=1}^{M} [(\tilde{f}g)_h]_i = 0 \tag{C3}$$

$$\sum_{i=1}^{M} [(\tilde{f}g)_h]_i \, h_i = - \sum_{i=1}^{M} f_i \, \tilde{g}_i. \tag{C4}$$

A finite differencing satisfying these constraints may be obtained by using a form of upstream differencing (see, e.g., Mesinger and Arakawa 1976). In particular a flux (F_i) at the thickness boundary h_i' for $i = 2$ to M is defined by

$$F_i = [\text{Max}(0, f_{i-1}) \, \tilde{g}_{i-1} + \text{Min}(0, f_i) \, \tilde{g}_i] \, / \, (h_i - h_{i-1}).$$

To ensure conditions C3 and C4, it is further insisted that

$$F_1 = F_{M+1} = 0.$$

Using these fluxes, the finite differences for the $(\tilde{f}g)_h$ term are

$$[(\tilde{f}g)_h]_i = \frac{F_{i+1} - F_i}{h_{i-1}' - h_i'}.$$

Multiplying both sides by $\Delta h = h_{i+1}' - h_i'$ gives

$$[(\tilde{f}g)_h]_i = F_{i-1} - F_i. \tag{C5}$$

The condition of eq C3 is satisfied since the F_i's cancel in pairs in the sum. To see that eq C4 is satisfied, consider an arbitrary growth rate, say $f_j \neq 0$. Then the left-hand side of eq C4 becomes

$$-F_j h_j + h_{j-1} F_{j-1} = \frac{f_j \tilde{g}_j (h_{j-1} - h_j)}{h_j - h_{j-1}} = -f_j \tilde{g}_j.$$

The exception to this occurs when open water is melting or the thickest category is freezing. In these cases the conditions $F_1 = F_{M+1} = 0$ prevent terms necessary for satisfying eq C4 from being included. However, in the case of open water melting this heat will be correctly accounted for by additional bottom or lateral melting as described earlier (see eq 5). To correct the thick ice freezing case, any growth over thick ice is reapportioned over the other growth rates in a manner similar to eq 5. In practice this amount can be made very small by taking the thick ice category to be very thick.

With this particular finite difference code (and dynamical code described previously) the essential stability requirement is a Courant-Friedrichs-Lewy condition for the advection terms, namely

48

$$\Delta t \le \Delta x \left[2|\psi|\right]^{-\frac{1}{2}}$$

for the spatial advection and

$$\Delta t \le |(h_i - h_{i-1})| \ \min \ \{[\text{Max}(0, f_{i-1})]^{-1}, \ -[\text{Min}(0, f_i)]^{-1}\}_{i=2, M-1}$$

for the thickness advection. Of these two terms the thickness advection term will normally be most critical.

Mechanical redistribution

Three mechanical redistribution operations are required at each time step in the numerical scheme. The operations consist of creating open water, carrying out an ice thickness redistribution and estimating the ice strength at the end of the time step. For the open water creation, all that are needed are finite differences for the strain rate tensor. These are calculated in a way identical to that used in the dynamical code and are described in Hibler (1979). (This reference also contains explicit expressions for the stress state σ_{ij} in terms of the strain rates and ice strength.) For the other two operations it is necessary to introduce finite differences for redistribution. For this purpose it is useful to define a discrete ridging operation.

Using the thickness partition notation introduced in Appendix A, one defines a discrete redistributor γ by

$$\tilde{\gamma}(h_i, h_j) = \int_{h_j'}^{h_{j+1}'} \gamma(h_i, h') \, dh' \qquad \text{for } j < M$$

$$\tilde{\gamma}(h_i, h_M) = \int_{h_M'}^{\infty} \gamma(h_i, h') \, dh'.$$

To ensure that $\tilde{\gamma}$ is normalized it is insisted that M

$$\sum_{i=1}^{M} \tilde{\gamma}(h_j, h_i) h_i = h_j.$$

In addition to $\tilde{\gamma}$ it is useful to define an auxiliary function λ_i by

$$\lambda_i = \sum_{j=1}^{M} \tilde{\gamma}(h_i, h_j).$$

Essentially, λ_i is the total reduction of area when a unit area of ice of thickness h_i is ridged.

To demonstrate how a redistribution is carried out, consider that an area reduction of

$$\Delta A = \sum_{i=1}^{M} \tilde{g}_i - 1$$

is required. To redistribute ice an initial set of category reductions (denoted by $\tilde{g}_i^0$) are estimated by

$$\widetilde{g}_i^* = \widetilde{g}_i \int_{h_i'}^{h_{i+1}'} P(h)\, dh.$$

In this integral g_i—in the definition of $P(h)$—is considered to be constant over the interval $h_i' + h_{i+1}'$. Defining $\Delta A'$ by

$$\Delta A' = \sum_{i=1}^{M} \lambda_i\, \widetilde{g}_i^*$$

a corrected set of category reductions are calculated by

$$\widetilde{g}_i^{**} + (\Delta A / \Delta A')\, \widetilde{g}_i^* .$$

The new $\widetilde{g}_i$'s are then given by

$$\widetilde{g}_i = \widetilde{g}_i - \widetilde{g}_i^{**} + \sum_{j=1}^{M} \widetilde{\gamma}(h_j, h_i)\, \widetilde{g}_j^{**}.$$

To estimate strengths, the simplest approach is to artificially enlarge all g values by, say, 0.1%. The potential energy is then calculated, a redistribution carried out, and a new potential energy calculated. The difference in potential energies divided by the strain then yields the ice strength.

Formally, this procedure consists of first defining

$$\widetilde{g}_i^* = 1.001\, \widetilde{g}_i.$$

As in Rothrock (1975), the initial potential energy is given by

$$S_i^* = C \sum_{i=1}^{M} \widetilde{g}_i^*\, h_i^2.$$

After redistribution $\widetilde{g}_i^*$ becomes $\widetilde{g}_i$ with potential energy

$$S_i = C \sum_{i=1}^{M} \widetilde{g}_i\, h_i^2.$$

Insisting that the compressive strength times the divergence rate equals the rate of potential energy change, one obtains the following equation for P^*:

$$P^* \frac{(0.001)}{\Delta t} = \frac{(S_i - S_i^*)}{\Delta t} .$$

In these expressions C is set equal to $2C_s$ to allow for frictional losses.

A facsimile catalog card in Library of Congress MARC
format is reproduced below.

END

FILMED

7-85

DTIC